AD-A212 001

FILE COPY

(2)

WRDC-TR-89-2025

COMPUTATION OF RAMJET INTERNAL FLOWFIELDS

James N. Scott
Wilbur L. Hankey
Thomas P. Gielda

University of Dayton
300 College Park
Dayton, OH 45469-0001

May 1989

Final Report For Period January 1986 - December 1988

Approved for public release; distribution is unlimited.

DTIC
ELECTE
SEP 07 1989
S B D

AEROPROPULSION AND POWER LABORATORY
WRIGHT RESEARCH AND DEVELOPMENT CENTER
AIR FORCE SYSTEMS COMMAND
WRIGHT-PATTERSON AIR FORCE BASE, OHIO 45433-6563

89 9 06 074

NOTICE

When Government drawings, specifications, or other data are used for any purpose other than in connection with a definitely Government-related procurement, the United States Government incurs no responsibility or any obligation whatsoever. The fact that the government may have formulated or in any way supplied the said drawings, specifications, or other data, is not to be regarded by implication, or otherwise in any manner construed, as licensing the holder, or any other person or corporation; or as conveying any rights or permission to manufacture, use, or sell any patented invention that may in any way be related thereto.

This report is releasable to the National Technical Information Service (NTIS). At NTIS, it will be available to the general public, including foreign nations.

This technical report has been reviewed and is approved for publication.

ABDOLLAH S. NEJAD, Proj Engr
Experimental Research Branch
Advanced Propulsion Division

JOHN T. HOJNACKI, Chief
Experimental Research Branch
Advanced Propulsion Division

FOR THE COMMANDER

WILLIAM G. BEECROFT, Director
Advanced Propulsion Division
Aero Propulsion & Power Laboratory

If your address has changed, if you wish to be removed from our mailing list, or if the addressee is no longer employed by your organization please notify WRDC/POPT, WPAFB, OH 45433-6563 to help us maintain a current mailing list.

Copies of this report should not be returned unless return is required by security considerations, contractual obligations, or notice on a specific document.

Unclassified
SECURITY CLASSIFICATION OF THIS PAGE

REPORT DOCUMENTATION PAGE

Form Approved
OMB No. 0704-0188

1a. REPORT SECURITY CLASSIFICATION Unclassified	1b. RESTRICTIVE MARKINGS
2a. SECURITY CLASSIFICATION AUTHORITY	3. DISTRIBUTION / AVAILABILITY OF REPORT Approved for Public release; Distribution is unlimited
2b. DECLASSIFICATION / DOWNGRADING SCHEDULE	
4. PERFORMING ORGANIZATION REPORT NUMBER(S)	5. MONITORING ORGANIZATION REPORT NUMBER(S) WRDC-TR-89-2025
6a. NAME OF PERFORMING ORGANIZATION The University of Dayton 6b. OFFICE SYMBOL (If applicable)	7a. NAME OF MONITORING ORGANIZATION Wright Research and Development Center Aero Propulsion & Power Laboratory (WRDC/POPT)
6c. ADDRESS (City, State, and ZIP Code) 300 College Park; Dayton, OH 45469-0001	7b. ADDRESS (City, State, and ZIP Code) WPAFB, 45433-6563
8a. NAME OF FUNDING / SPONSORING ORGANIZATION 8b. OFFICE SYMBOL (If applicable)	9. PROCUREMENT INSTRUMENT IDENTIFICATION NUMBER
8c. ADDRESS (City, State, and ZIP Code)	10. SOURCE OF FUNDING NUMBERS

PROGRAM ELEMENT NO.	PROJECT NO.	TASK NO	WORK UNIT ACCESSION NO.
61102F	2308	51	17

11. TITLE (Include Security Classification)

Computation of Ramjet Internal Flowfields

12. PERSONAL AUTHOR(S)

James N. Scott, Wilbur L. Hankey, Thomas P. Gielda

13a. TYPE OF REPORT	13b. TIME COVERED	14. DATE OF REPORT (Year, Month, Day)	15. PAGE COUNT
Final	FROM 1/86 TO 12/88	May 1989	93

16. SUPPLEMENTARY NOTATION

17. COSATI CODES		
FIELD	GROUP	SUB-GROUP
21	01	
20	04	

18. SUBJECT TERMS (Continue on reverse if necessary and identify by block number)

PNS	Combustion	Subsonic
Ramjet	CFD	Supersonic
Scramjet	Internal Flowfield	Computational Fluid Dynamics (CFD)

19. ABSTRACT (Continue on reverse if necessary and identify by block number)

This document reports on the computation of Ramjet Internal Flowfields. It is divided into two sections, i.e. subsonic and supersonic combustion. To numerically simulate subsonic combustion the time-dependent Navier-Stokes equations are used with additional species equations incorporated to model hydrocarbon-air combustion.

To compute supersonic combustion the parabolized Navier-Stokes equations are utilized (PNS) with species equations to simulate hydrogen-air combustion. Model cases are computed and compared with limited experimental data. Keywords:

20. DISTRIBUTION / AVAILABILITY OF ABSTRACT ☒ UNCLASSIFIED/UNLIMITED ☐ SAME AS RPT. ☐ DTIC USERS	21. ABSTRACT SECURITY CLASSIFICATION Unclassified
22a. NAME OF RESPONSIBLE INDIVIDUAL A. S. Nejad	22b. TELEPHONE (Include Area Code) 513-255-1234 22c. OFFICE SYMBOL WRDC/POPT

DD Form 1473, JUN 86 Previous editions are obsolete. SECURITY CLASSIFICATION OF THIS PAGE

TABLE OF CONTENTS

SECTION		PAGE
1	INTRODUCTION	1
2	R&D STATUS REPORT	1
	2.1 Subsonic Combustion	1
	2.1.1 Governing Equations	1
	2.1.2 Transport Properties of a Mixture	2
	2.1.3 Thermodynamic Properties	3
	2.1.4 Reaction Rate Model	6
	2.1.5 Initial Values	7
	2.1.6 Equilibrium Chemistry	8
	2.1.7 Model Problems for Subsonic Combustion	14
	2.1.7.1 Cold Flow Computations	14
	2.1.7.1.1 Computational Grid	18
	2.1.7.1.2 Numerical Results	20
	2.1.7.2 Quasi-One-Dimensional Model Problem	28
	2.1.7.2.1 Governing Equations	28
	2.1.7.2.2 Initial and Boundary Conditions	29
	2.1.7.2.3 Results	31
	2.2 Supersonic Combustion	31
	2.2.1 Governing Equations	38
	2.2.2 Numerical Method	42
	2.2.3 Initial and Boundary Conditions	43
	2.2.4 Numerical Smoothing	44
	2.2.5 Reaction Rate Modeling	47
	2.2.6 Finite Rate Model	48
	2.2.7 Equilibrium Reaction Rate Modeling	48
	2.2.8 Equilibrium Chemistry	50
	2.2.9 Heats of Formation	53
	2.2.10 Model Problems for Supersonic Combustion	53
	2.2.10.1 Non Reacting Flow Over Compression Ramp	57
	2.2.10.2 Experiment of Burrows and Kurkov	59
3	SUMMARY	71
	REFERENCES	73
	APPENDIX	75

QUALITY INSPECTED 4

Codes
Avail and/or
Dist Special
A-1

LIST OF ILLUSTRATIONS

FIGURE		PAGE
1	Dump combustor configuration.	16
2	Boundary conditions for dump combustor configuration.	19
3	Pressure histograms - coarse grid.	21
4	Pressure histograms - medium grid.	22
5	Pressure histograms - fine grid.	23
6	Experimental pressure histograms.	24
7	Shedding phenomena.	26
8	Reattachment phenomena.	27
9	Shock induced deflagration model problem. Quasi-One-Dimensional.	30
10	Axial pressure profile (Reacting Flow) - with increased stress damping.	32
11	Axial pressure profile (Nonreacting Flow).	33
12	Axial pressure profile (Reacting Flow) - with normal stress damping.	34
13	Axial temperature profile (Reacting Flow).	35
14	Axial temperature profile (Nonreacting Flow).	36
15	Axial mass fractions (Reacting flow).	37
16	Computed surface pressure on a secant-ogive-cylinder-boat-tail projectile (without normal stress damping).	45
17	Computed surface pressure on a secant-ogive-cylinder-boat-tail projectile (with normal stress damping).	46
18	Effect of temperature on overall heat of combustion.	56
19	Ramp configuration for Holden's test cases.	58

FIGURE		PAGE
20	Wall C_p as a function of x. Holden's test conditions.	60
21	Comparison of heat transfer coefficients for Holden's test case.	61
22	Schematic of the Burrows-Kurkov experimental apparatus.	62
23	Computed pressure contours from the SSCPNS computer code (finite rate chemistry).	64
24	Computed pressure contours from the SSCPNSEQ computer code (equilibrium reaction rate model).	65
25	Computed temperature contours from SSCPNS.	66
26	Computed temperature contours from SSCPNSEQ.	67
27	Comparison of computed and experimentally measured species mole fractions from SSCPNS.	68
28	Comparison of computed and experimentally measured species mole fractions from SSCPNSEQ.	69
29	Comparison of computed and measured total temperature profiles. Varma's reaction rate model.	70

LIST OF TABLES

TABLE		PAGE
1	Summary of JANNAF Tables of Thermochemical Data.	6
2	Summary of Mass Fractions Entering the Combustor Region.	8
3	Hydrocarbon-Air Combustion.	12
4	Mole Fractions and Mass Fractions.	13
5	Summary of Computations.	20
6	Species and Reactions.	49
7	Hydrogen-Air Combustion.	54
8	Heats of Formation.	55

1. INTRODUCTION

Current Air Force interest is high on ramjet technology due to the advent of the National Aerospace Plane project (NASP). The aerodynamic community is experiencing an exponential growth in Computational Fluid Dynamics (CFD) as witnessed by the large number of publications now appearing in this field. It is, therefore, appropriate that CFD methodology be brought to bear on the ramjet technology. By numerical modeling the flow process and conducting validating experiments the ramjet field may be advanced. This report documents work on the Aero Propulsion Laboratory Contract (No. F33615-86-C-2615) on the computation of Ramjet Internal Flowfields.

2. R&D STATUS REPORT

The CFD effort on Ramjet Internal Flowfields may be divided into two categories, i.e. subsonic combustion and supersonic combustion. The first category (subsonic) employs the time-dependent Navier-Stokes code and adds the species equations for hydrocarbon fuel and air combustion. A forward reaction rate model is used for the complete chemical reaction. The second category (supersonic) utilizes the parabolized Navier-Stokes program with additional species equations for hydrogen/air combustion. The "extent of reaction" method is used to account for equilibrium chemistry. These two categories now will be discussed.

2.1 Subsonic Combustion

2.1.1 Governing Equations

The governing equations for combustion driven flows include the conservation of species, momentum and energy, plus the state equation. These are listed below in conservation form:

$$\frac{\partial \rho Y_i}{\partial t} + \nabla \cdot (\rho Y_i \underline{V} - \rho D_{ij} \nabla Y_i) = \dot{m}_i$$

$$\frac{\partial \rho \underline{V}}{\partial t} + \nabla \cdot (\rho \underline{V}\underline{V} - \underline{\underline{\tau}}) = 0$$

$$\frac{\partial \rho e}{\partial t} + \nabla \cdot (\rho \underline{V} e - \underline{\underline{\tau}} \cdot \underline{V} - \dot{\underline{q}}) = 0$$

$$p = \sum p_i = \rho RT \sum \frac{Y_i}{M_i} \quad ; \quad h = \sum Y_i h_i \quad ; \quad \sum Y_i = 1$$

where

$$\underline{\underline{\tau}} = -(p + \frac{2}{3} \mu \nabla \cdot \underline{V}) \underline{\underline{I}} + \mu (\nabla \underline{V} + \underline{V} \nabla)$$

$$e = h + \frac{V^2}{2} - \frac{p}{\rho}$$

$$\dot{\underline{q}} = k \nabla T + \sum \rho D_{ij} h_i \nabla Y_i$$

$$\frac{\mu}{\rho D_{ij}} = S_{c_i} \quad ; \quad \frac{\mu C_p}{k} = P_r$$

$$h_i = \int Cp_i dT + h_i^o$$

$$\dot{m}_i = -k_i \, e^{-E_i/RT} \, (\rho_i^{\nu_i})(\rho_j^{\nu_j}) \text{ Arrhenius Law}$$

$$\dot{m}_j = S_j \dot{m}_1 \quad , \quad S_j = \text{Stoichiometric Coefficient}$$

2.1.2 Transport Properties of a Mixture

To solve the conservation equations for a mixture of gases the transport coefficients (μ, k, D_{ij}) are required. A method for determining these coefficients has been reported by Wilke[1], however, for the subsonic ramjet in which 75 percent of the mixture is nitrogen, the following, simpler, procedure will be used.

Sutherland's law for viscosity:

$$\bar{\mu} = \mu_r \left(\frac{T^{\frac{3}{2}}}{T + S} \right)$$

where $\mu_r = 2.27 \times 10^{-8} \frac{lb\ sec}{ft^2}$ air values

$$S = 198.6°R$$

$$\bar{k} = \frac{\bar{\mu}\bar{C}_p}{P_r}$$

$$\rho D_{ij} = \frac{\bar{\mu}}{S_{c_i}}$$

For T = 1,800°R, Kanury[2] presents the following values for air.

$$P_r \approx 0.70$$

$$S_c \approx 1.00$$

(Note this corresponds to a Lewis number, $Le = \frac{S_c}{P_r} = 1.4$.) These values appear appropriate for the early calculations. The values for the molecular transport phenomena are masked by the unsteady convection transport being simulated by the time-dependent oscillations. Therefore, the computation is relatively insensitive to the values of these molecular transport coefficients.

2.1.3 Thermodynamic Properties

In the CFD codes involving different gas species at elevated temperatures there is a need to evaluate the thermodynamic properties as a function of temperature. The procedure should be as simple as possible and not require iteration.

The conservation equations provide the following information at each point in time and space.

$$\rho,\ \rho u,\ \rho v,\ \rho w,\ \rho e,\ \rho Y_i$$

From this information it is necessary to determine p and T. The following equations provide this information:

$$p = \sum p_i \text{ where } p_i = \frac{Y_i}{M_i} \rho RT$$

where $R = 1.987$ cal/(gm mole)°K or $49{,}723 \dfrac{ft^2}{sec^2 \cdot R \text{ mole}}$

M_i = molecular weight

Hence $p = \rho \bar{R} T$ where $\bar{R} = \sum \dfrac{Y_i}{M_i} R$.

The temperature must be obtained from enthalpy.

$$h = \sum Y_i h_i$$

$$h_i = \int_0^T C_{p_i} dT + h_i^o$$

$$C_{p_i} = \frac{C_{p_i}}{M_i} \text{ (based on mass)}$$

C_{p_i} = specific heat at constant pressure (based on mole)

Therefore,

$$h = \bar{C}_p T + \sum Y_i h_i^o$$

where

$$\bar{C}_p = \sum \frac{Y_i}{T} \int_0^T C_{p_i} dT$$

Hence, temperature may be deduced from the known value of internal energy (e).

$$e = h - \frac{p}{\rho} + \frac{V^2}{2} = \bar{C}_p T + \sum Y_i h_i^o - \bar{R}T + \frac{V^2}{2}$$

or $$T = \frac{e - \frac{V^2}{2} - \sum Y_i h_i^o}{\bar{C}_p - \bar{R}}$$

The complexity in this equation is due to the fact that $\bar{C}_p$ is a function of T, requiring an iteration to resolve. Several methods of solution are possible, each with different computational efficiency. The simplest method is to evaluate $\bar{C}_p$ at time $(t - \Delta t)$ to find $T(t)$. The alternate approach is to solve a low order polynomial for the positive real root. To obtain $\bar{C}_p(T)$ a quadratic polynomial for the C_{p_i} for each species was derived. Using the JANNAF Tables of Thermochemical Data,[3] a best fit for the five species involved in the combustion of JP-4 and air was accomplished over the temperature range from 900° to 4,500°R.

$$C_{p_i} = a_i + b_i T + c_i T^2$$

These values are tabulated in Table 1. The global value for $\bar{C}_p$ may be obtained by the following integration:

$$\bar{C}_p = \sum \frac{Y_i}{T} \int_0^T C_{p_i} dT = \sum Y_i a_i + \frac{T}{2} \sum Y_i b_i + \frac{T^2}{3} \sum Y_i c_i$$

Each species will require seven quantities to determine all property values. For hydrocarbon combustion over a temperature range from 900° to 4,500°R the values in Table 1 are appropriate.

TABLE 1

SUMMARY OF JANNAF TABLES OF THERMOCHEMICAL DATA

Species	M_i	$C_p = a_i + b_iT + c_iT^2$ $ft^2/sec^2 \cdot R$			ft^2/sec^2	$\dot{m}_j = S_j\dot{m}_1$
		a_i	b_i	c_i	$*h_i^o$	S_i
CH_2	14	10,740	6.396	-7.46×10^{-4}	-0.160×10^{8}	1.00
O_2	32	5,156	0.927	-1.09×10^{-4}	0	+3.429
CO_2	44	3,623	2.913	-4.48×10^{-4}	-0.964×10^{8}	-3.143
H_2O	18	10,342	1.856	0	-1.450×10^{8}	-1.286
N_2	28	5,997	0.517	0	0	0

$R = 49{,}732\ ft^2/sec^2 \cdot R$ mole, $P_r = 0.70$, and $R_i = \frac{R}{M_i}$

*This corresponds to 18.9 kBtu/lbm fuel.

2.1.4 Reaction Rate Model

As stated previously, an Arrhenius Law reaction model was used for the combustion of a hydrocarbon. Locally the following chemical equation prevails.

$$CH_2 + 1.5\ O_2 \rightarrow CO_2 + H_2O$$

The following reaction rate model is used to describe the reduction of the hydrocarbon.

$$\dot{m}_1 = -k_1 e^{\frac{E_1}{\bar{R}T}} (\rho Y_1)(\rho Y_2)^{1.5}$$

where

$$\frac{E_1}{\bar{R}} = 26{,}000^0\text{R activation temperature}$$

$$k_1 = 10^{18}/[\frac{\text{slugs}}{\text{ft}^3}]^{1.5} \text{ sec}$$

The remaining species production will be determined from the stoichiometric coefficients (S_j) and $\dot{m}_1$.

$$\dot{m}_j = S_j \dot{m}_1$$

The values of S_j are listed in Table 1.

2.1.5 Initial Values

Two time-dependent computations for combustion in the model ramjet were accomplished. The initial conditions for the cases were: T_0 = 1,000°R, P_0 = 33 psia at fuel-air ratios of .020 and .032. The mixture entering the combustor is vitiated air which has been heated to 1,000°R by burning hydrocarbon fuel. The nitrogen/oxygen ratio is returned to 3.76 (by volume) by adding O_2.

A summary of the mass fractions, for the five species of interest, entering the combustor region for the two cases is shown in Table 2.

The upstream boundary conditions are:

$$P_0 = 33 \text{ psia} = 4{,}752 \text{ psf} \qquad v = 0$$

$$T_0 = 1{,}000°\text{R} \qquad \frac{du}{dx} = 0$$

TABLE 2
SUMMARY OF MASS FRACTIONS
ENTERING THE COMBUSTOR REGION

Species	$\phi f = 0.020$ Y_i	$\phi f = 0.032$ Y_i
CH_2	0.020	0.032
O_2	0.222	0.219
CO_2	0.018	0.018
H_2O	0.007	0.007
N_2	0.733	0.724
	$\sum Y_i = 1.000$	$\sum Y_i = 1.000$

2.1.6 Equilibrium Chemistry

Before devising a scheme to represent a combustion model it is necessary to examine the equilibrium state at the anticipated final condition. In this manner the appropriate species may be identified.

The classical procedure involves the use of mole fractions and was used in this analysis, even though the CFD code employs mass fractions. The mole fractions of the equilibrium composition of the products of combustion of $(CH_2)_k$ are determined using the equations involving equilibrium constants with the assumption that the component gases obey the equation of state for an ideal gas.

$$p_i = \frac{\rho_i}{M_i} RT$$

For the combustion of a hydrocarbon fuel at various equivalence ratios the general chemical reaction involving ten species for products may be written as follows:

$$\frac{1}{k}(CH_2)_k + \frac{1.5}{\phi}(O_2 + 3.76\ N_2) \rightarrow$$

$$n_{N_2}(N_2) + n_{O_2}(O_2) + n_{CO_2}(CO_2) + n_{H_2O}(H_2O) + n_{NO}(NO) +$$

$$n_{OH}(OH) + n_{CO}(CO) + n_{H_2}(H_2) + n_H(H) + n_O(O)$$

where n_i = number of moles of product "i"

ϕ = equivalence ratio - the actual fuel-air ratio relative to a stoichiometric fuel-air ratio.

Air was presumed to be composed of 79 percent N_2 and 21 percent O_2 by volume (i.e., $\frac{.79}{.21} = 3.76$).

Four elements are involved (C, O, H, N) and hence four conservation of chemical species equations may be specified.

C: $1 = n_{CO_2} + n_{CO}$

O: $2(\frac{1.5}{\phi}) = 2n_{O_2} + 2n_{CO_2} + n_{H_2O} + n_{NO} + n_{OH} + n_{CO} + n_O$

H: $2 = 2n_{H_2O} + n_{OH} + 2n_{H_2} + n_H$

N: $2(\frac{1.5}{\phi})3.76 = 2n_{N_2} + n_{NO}$

Since there are 10 unknown molar species values, 6 equilibrium constants are required to solve the system.

$$K_{CO_2} = \frac{K_{P,CO_2}}{K_{P,CO}}\sqrt{\frac{P}{n}} = \frac{n_{CO_2}}{\sqrt{n_{CO}}\sqrt{n_{O_2}}}$$

$$K_{H_2O} = K_{P,H_2O}\sqrt{\frac{P}{n}} = \frac{n_{H_2O}}{\sqrt{n_{H_2}}\sqrt{n_{O_2}}}$$

$$K_{OH} = K_{P,OH} = \frac{n_{OH}}{\sqrt{n_{H_2}}\sqrt{n_{O_2}}}$$

$$K_{NO} = K_{P,NO} = \frac{n_{NO}}{\sqrt{n_{N_2}}\sqrt{n_{O_2}}}$$

$$K_H = K_{P,H}\sqrt{\frac{n}{P}} = \frac{n_H}{\sqrt{n_{H_2}}}$$

$$K_O = K_{P,O}\sqrt{\frac{n}{P}} = \frac{n_O}{\sqrt{n_{O_2}}}$$

where $K_{P,i} = f(T)$ from JANNAF Tables. Two additional variables are introduced in these equations, i.e., p and n. $p = \text{pressure} = \sum p_i$ and must be specified. $n = \sum n_i$ = total number of moles of the combustion products and becomes an auxiliary equation.

The problem has now been formulated. Given ϕ, p, and T there exists 11 algebraic equations involving 10 molar values (n_i) plus the total number of moles (n). Conceptually, this system of equations could be reduced to a single very high degree polynomial. Physical reasoning requires that only one positive real root exist. In practice the system is reduced to fewer equations by substitution.

The following iteration sequence was used to resolve the current problem:

$$n_{N_2} = \frac{5.64}{\phi} - \frac{1}{2}\, n_{NO}$$

$$n_{O_2} = \frac{1}{2}\left(\frac{3}{\phi} - 2\right) - \frac{1}{2}\, n_{CO_2} + \frac{1}{2}\left(n_{H_2} + \frac{1}{2}\, n_H - \frac{1}{2}\, n_{OH} - n_{NO} - n_O\right)$$

$$n_{H_2} = \frac{1 - \frac{1}{2}(n_{OH} + n_H)}{1 + K_{H_2O}\sqrt{n_{O_2}}}$$

$$n_{NO} = K_{NO}\sqrt{n_{N_2}}\sqrt{n_{O_2}}$$

$$n_{OH} = K_{OH}\sqrt{n_{H_2}}\sqrt{n_{O_2}}$$

$$n_H = K_H\sqrt{n_{H_2}}$$

$$n_O = K_O\sqrt{n_{O_2}}$$

$$n_{H_2O} = 1 - n_{H_2} - \frac{1}{2}(n_{OH} + n_H)$$

$$n_{CO_2} = \left[1 + \frac{1}{K_{CO_2}\sqrt{n_{O_2}}}\right]^{-1}$$

$$n_{CO} = 1 - n_{CO_2}$$

$$n = \sum n_i$$

An example problem has been solved for $\phi = 0.6$ and $p = 2$ atmospheres at a temperature range of 900° to 4,500°R. This state approximates the ramjet combustor condition. A summary of the result is shown in Tables 3 and 4.

An analysis of equilibrium chemistry for hydrocarbon combustion in a ramjet has been accomplished. It was demonstrated that all products of combustion beyond the basic species of N_2, O_2, H_2O, and CO_2 occur at traces less than one percent for temperatures below 4,140°F. Based upon this analysis it appears satisfactory to use a single-step global reaction of the following form*:

$$\frac{1}{k}(CH_2)_k + \frac{1.5}{\phi}(O_2 + 3.76\ N_2) \rightarrow$$

$$\left(\frac{1.5}{\phi}\right)3.76\ N_2 + 1.5\left(\frac{1}{\phi} - 1\right)O_2 + CO_2 + H_2O$$

*Note: $\phi < 1$ for a lean mixture.

TABLE 3
HYDROCARBON-AIR COMBUSTION

$\phi = 0.6$ Equilibrium States $p = 2$ atmospheres			
	T = 2,700°R	T = 3,600°R	T = 4,500° R
K_{CO_2}	$\frac{2.93}{\sqrt{n}} \times 10^5$	$\frac{1,083}{\sqrt{n}}$	$\frac{38.9}{\sqrt{n}}$
K_{H_2O}	$\frac{7.51}{\sqrt{n}} \times 10^5$	$\frac{4,903}{\sqrt{n}}$	$\frac{237}{\sqrt{n}}$
K_{NO}	0.00326	0.0200	0.0593
K_{OH}	0.263	0.558	0.871
K_H	$1.24\sqrt{n} \times 10^{-5}$	$0.00115\sqrt{n}$	$0.0177\sqrt{n}$
K_O	$2.85\sqrt{n} \times 10^{-6}$	$4.7 \times 10^{-4}\sqrt{n}$	$0.0102\sqrt{n}$
n_{N_2}	9.400	9.370	9.313
n_{H_2O}	0.9997	0.992	0.931
n_{O_2}	0.998	0.967	0.923
n_{CO_2}	1.000	0.997	0.914
n_{NO}	9.98×10^{-3}	0.0602	0.174
n_{OH}	5.70×10^{-4}	0.0148	0.101
n_{CO}	1.20×10^{-5}	0.00330	0.0864
n_O	1.00×10^{-5}	0.00163	0.0347
n_{H_2}	4.7×10^{-6}	7.25×10^{-4}	0.0145
n_H	9.5×10^{-8}	1.09×10^{-4}	0.0075
n	12.408	12.407	12.499

TABLE 4

MOLE FRACTIONS

ϕ = 0.6	X_i	P = 2 atmospheres		
Species	T = 2,700°R	T = 3,600°R	T = 4,500°R	M_i
N_2	0.758	0.755	0.745	28
H_2O	0.0806	0.0800	0.0747	18
O_2	0.0802	0.0779	0.0739	32
CO_2	0.0806	0.0804	0.0731	44
NO	0.0008	0.0049	0.0139	30
OH	0.00006	0.0012	0.0078	17
CO	----	0.0003	0.0069	28
O	----	0.0001	0.0028	16
H_2	----	----	0.0011	2
H	----	----	0.0006	1.0

MASS FRACTIONS

	Y_i		
Species	T = 2,700°R	T = 3,600°R	T = 4,500°R
N_2	0.737	0.738	0.730
CO_2	0.123	0.124	0.113
O_2	0.089	0.087	0.083
H_2O	0.050	0.050	0.047
NO	0.001	0.005	0.015
OH	0.3×10^{-5}	0.001	0.005
CO	---	---	0.007
O	---	---	0.002
H_2	---	---	---
H	---	---	---

This, therefore, negates the need for the equilibrium constants and greatly simplifies the numerical computations. However, as a check on this model, equilibrium conditions can be computed at different states, after the fact, to confirm this approach. Additional discussion of computational procedures for equilibrium chemistry is presented in the Appendix.

2.1.7 Model Problems for Subsonic Combustion

To validate the chemically reacting program two model problems were accomplished. The first was the simulation of cold flow in the dump combustor for a case in which experimental data existed. This model problem demonstrates the capability to simulate the fluid mechanical features. The second selected was the case for quasi-one-dimensional flow with subsonic deflagration of ten percent equivalence ratio of premixed methane gas and air. This second case activates the chemistry features of the code. The results of these numerical investigations follow.

2.1.7.1 Cold Flow Computations

In preparation to performing computations for a chemically reacting flowfield, it is imperative that the computer code have the capability to perform computations for the non-reacting test case. These cold flow computations were made in a previous investigation conducted at UDRI (Contract F33615-81-C-2078, Task 019). Difficulty was encountered, however, in obtaining agreement with experiment. The principal discrepancies between the computed solutions and the experimental data were:

1. The computed streamlines did not reattach in the location measured in experiment.
2. The computed average inlet Mach number was higher than the value calculated in experiment.
3. The computed frequency of the self-excited oscillation was approximately twice the value measured in experiment.

In the previous investigation attempts were made to improve the accuracy of the computed solutions by various means including:

1. Performing computations with increased grid resolutions in the radial direction.

2. Performing computations with various forms of algebraic turbulence models.

Based on the results of the previous investigation, it was deemed necessary to perform a series of numerical experiments while varying the axial resolution of the computational grid. It is important that the computational grid have sufficient resolution in the axial directions to resolve the large scale vortical structures. It was hypothesized and later verified by computation that by increasing the resolution in the axial direction the large scale vortical structures would be resolved. Resolution of the large scale structures would allow more kinetic energy of the flow to be dissipated through vorticity. This decrease in kinetic energy of the flow would result in reattachment in a region closer to the reattachment point measured by experiment. The reattachment point computed in the previous investigation was located on the downstream choke nozzle (see Figure 1) (i.e., the computed field streamlines flow never reattached in the dump combustor).

The configuration of the ramjet dump combustor is shown in Figure 1. This configuration is axisymmetric, hence, the axisymmetric forms of the time-dependent Navier-Stokes equations can be used. Note for the nonreacting case the species equations are dropped from the analysis.

$$U_t + E_x + (1/r)(rF)_r = H$$

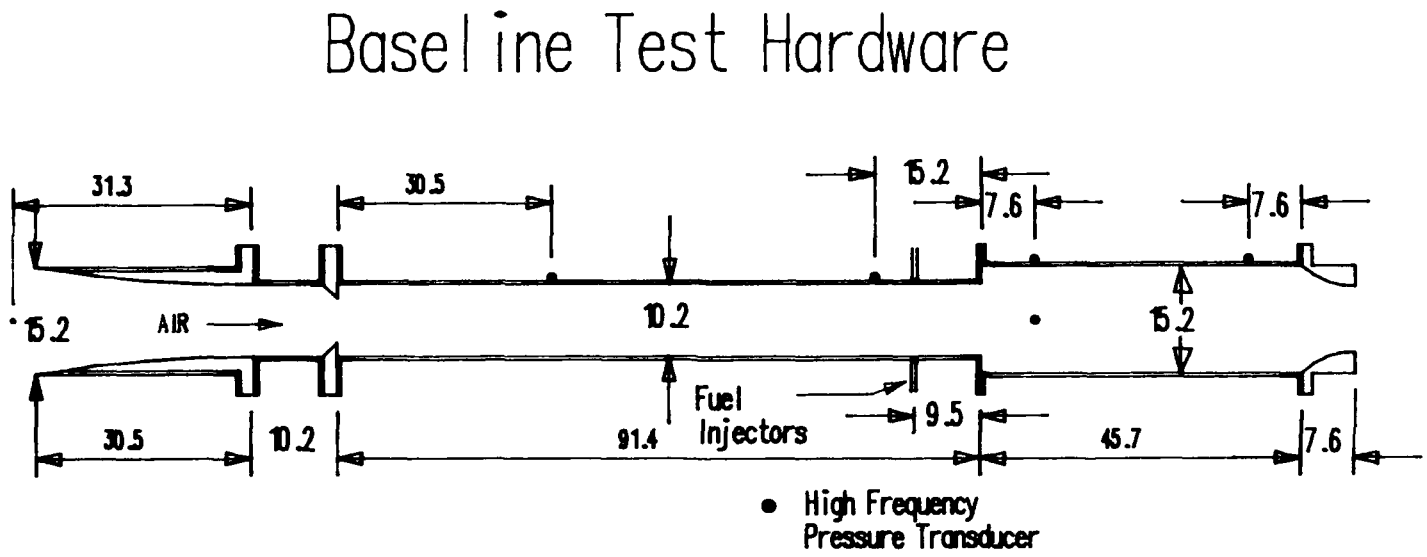

Figure 1. Dump combustor configuration.
(All lengths in cm.)

where

$$U = \begin{bmatrix} \rho \\ \rho u \\ \rho v \\ \rho e \end{bmatrix}$$

$$E = \begin{bmatrix} \rho u \\ \rho u^2 - \sigma_{xx} \\ \rho uv - \tau_{xr} \\ \rho ue - u\sigma_{xx} - v\tau_{rx} - kT_x \end{bmatrix}$$

$$F = \begin{bmatrix} \rho v \\ \rho uv - \tau_{rx} \\ \rho v^2 - \sigma_{rr} \\ \rho ve - v\sigma_{rr} - u\tau_{xr} - kT_r \end{bmatrix}$$

$$H = \begin{bmatrix} 0 \\ 0 \\ -\tau_{\theta\theta}/r \\ 0 \end{bmatrix}$$

and where the components of the stress tensor are given by

$$\sigma_{xx} = (2\mu + \lambda)\frac{\partial u}{\partial x} + \lambda \left[\frac{v}{r} + \frac{\partial v}{\partial r}\right] - p$$

$$\sigma_{rr} = (2\mu + \lambda)\frac{\partial u}{\partial r} + \lambda \left[\frac{v}{r} + \frac{\partial u}{\partial x}\right] - p$$

$$\tau_{\theta\theta} = (2\mu + \lambda)\frac{v}{r} + \lambda \left[\frac{\partial u}{\partial x} + \frac{\partial v}{\partial r}\right] - p$$

$$\tau_{xr} = \tau_{rx} = \mu\left[\frac{\partial u}{\partial r} + \frac{\partial v}{\partial x}\right]$$

The dependent variables for this system of equations are $U(\rho, \rho u, \rho v, \rho e)$. Sutherland's viscosity equation, the equation of state, and the Prandtl number are specified to close this system of equations.

For the present investigation, the no-slip boundary conditions are applied at the outer duct walls and a symmetry boundary condition is applied at the duct centerline.

Treatment of the inflow and outflow conditions are among the primary focuses of this investigation. These conditions consist of the following:

Subsonic Inflow: P_0, T_0, $v = 0$ specified

$$\frac{\partial(\rho u)}{\partial x} = 0$$

Supersonic Outflow: $\frac{\partial u}{\partial x} = \frac{\partial v}{\partial x} = \frac{\partial T}{\partial x} = \frac{\partial p}{\partial x} = 0$

These conditions are shown in Figure 2.

2.1.7.1.1 Computational Grid

To study the effects of axial grid resolution on self-excited oscillating flows a series of computations were performed by employing grids with various axial spacing and comparisons were made with experiment for three computational grids.

- Grid 1 - 74 axial × 41 radial points (coarse)
- Grid 2 - 151 axial × 41 radial points (medium)
- Grid 3 - 301 axial × 41 radial points (fine)

The axial spacing for the coarse grid was exponentially stretched with a minimum Δx of 0.2 inch at the dump plane and a maximum Δx of 0.5 inch near the throat of the downstream choke nozzle. The axial spacing for the medium and fine grids was constant at $\Delta x = 0.2$ and 0.1 inch, respectively. All of the computations were made with the axisymmetric unsteady Navier-Stokes code first developed by Shang.[4]

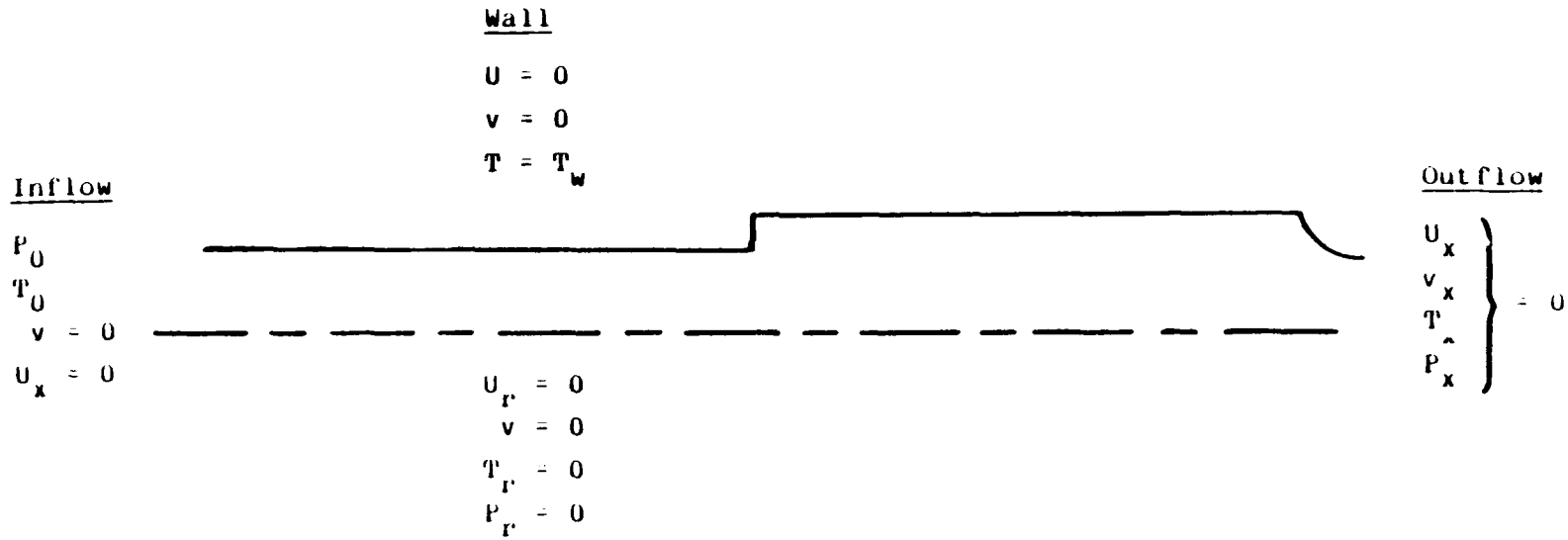

Figure 2. Boundary conditions for dump combustor configuration.

2.1.7.1.2 Numerical Results

Computations were performed for the experimental ramjet configuration shown in Figure 1. The Reynolds number based on inlet pipe diameter was 1.0×10^6. The average static pressure and Mach number upstreams of the dump plane were 1,570 psf and 0.55, respectively. The total temperature, specified at the upstream boundary condition, and the wall temperature were held constant at 522°R.

Computed pressure histograms at locations P_4, P_6, and P_{10} (reference Figure 1) for the coarse, medium, and fine computational grids are shown in Figures 3, 4, and 5, respectively. The results of the experimental measurements taken in the dump combustor for the above test conditions are shown in Figure 6. The increase in grid point density has a dramatic impact on the pressure histograms, especially from the coarse to medium grid. As the resolution in the axial direction is refined, the computed results approach the experimental data (see Table 5) where $\bar{A}$ and $\bar{f}$ are the average peak to peak amplitude and average frequency respectively.

TABLE 5

SUMMARY OF COMPUTATIONS

Axial Grid Points	$\bar{P}_4$	$\bar{A}_4$	$\bar{f}_4$(Hz)	M Inlet
71	1,306	125	357	0.77
151	1,405	320	340	0.63
301	1,409	320	303	0.59
Experiment	1,570	202	190	0.55

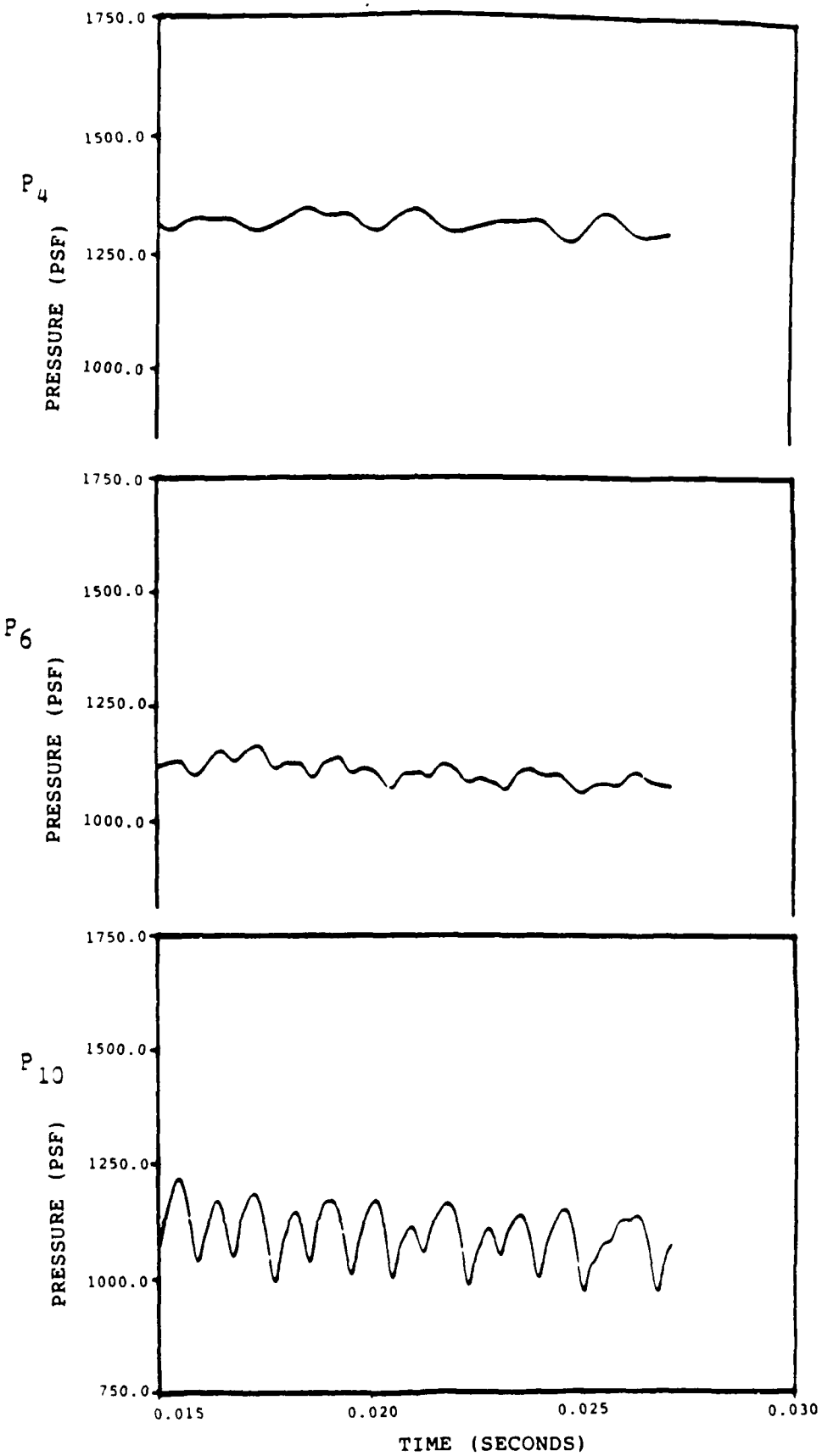

Figure 3. Pressure histograms--coarse grid (71 x 41).

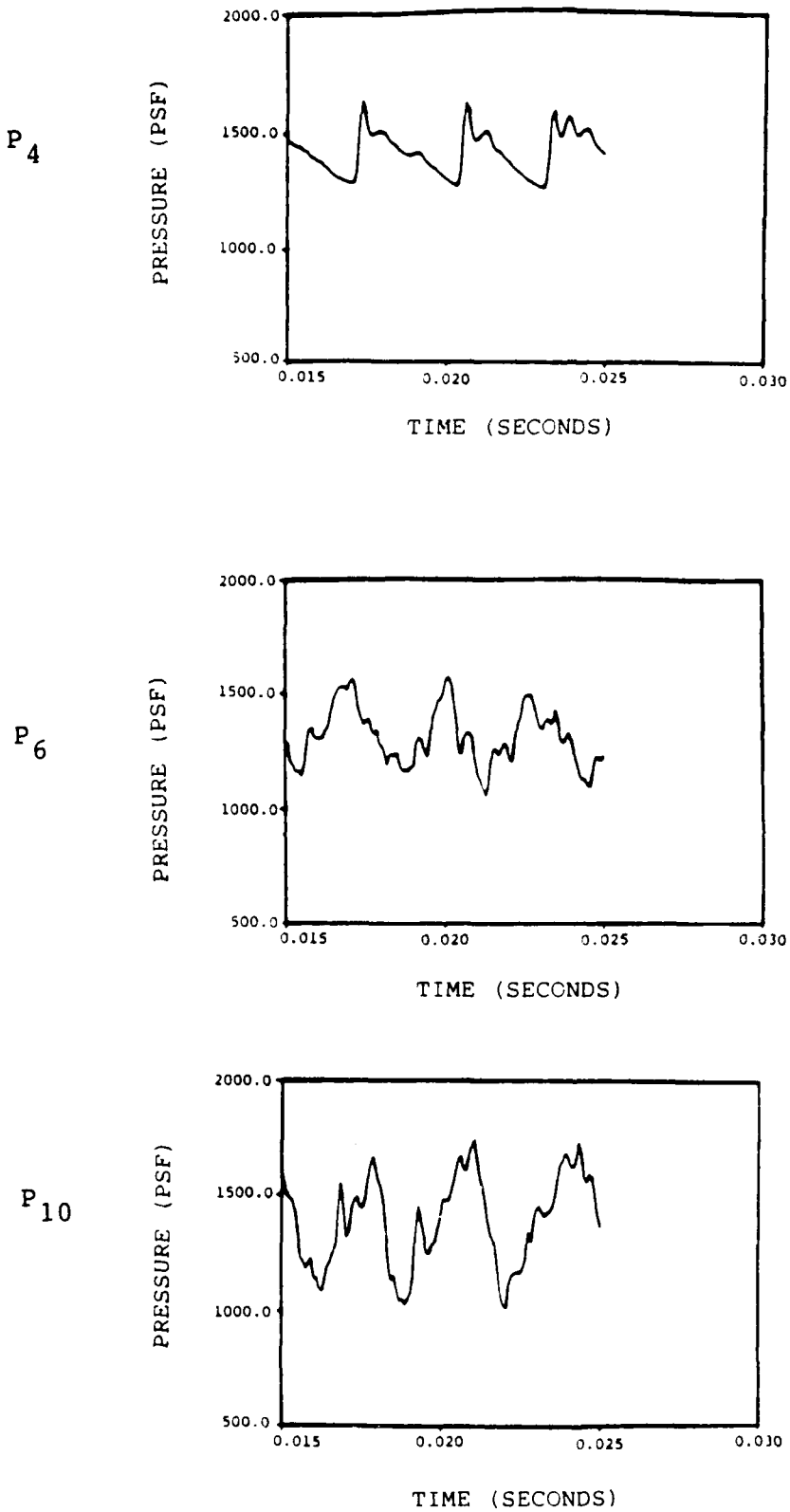

Figure 4. Pressure histograms--medium grid (151 x 41).

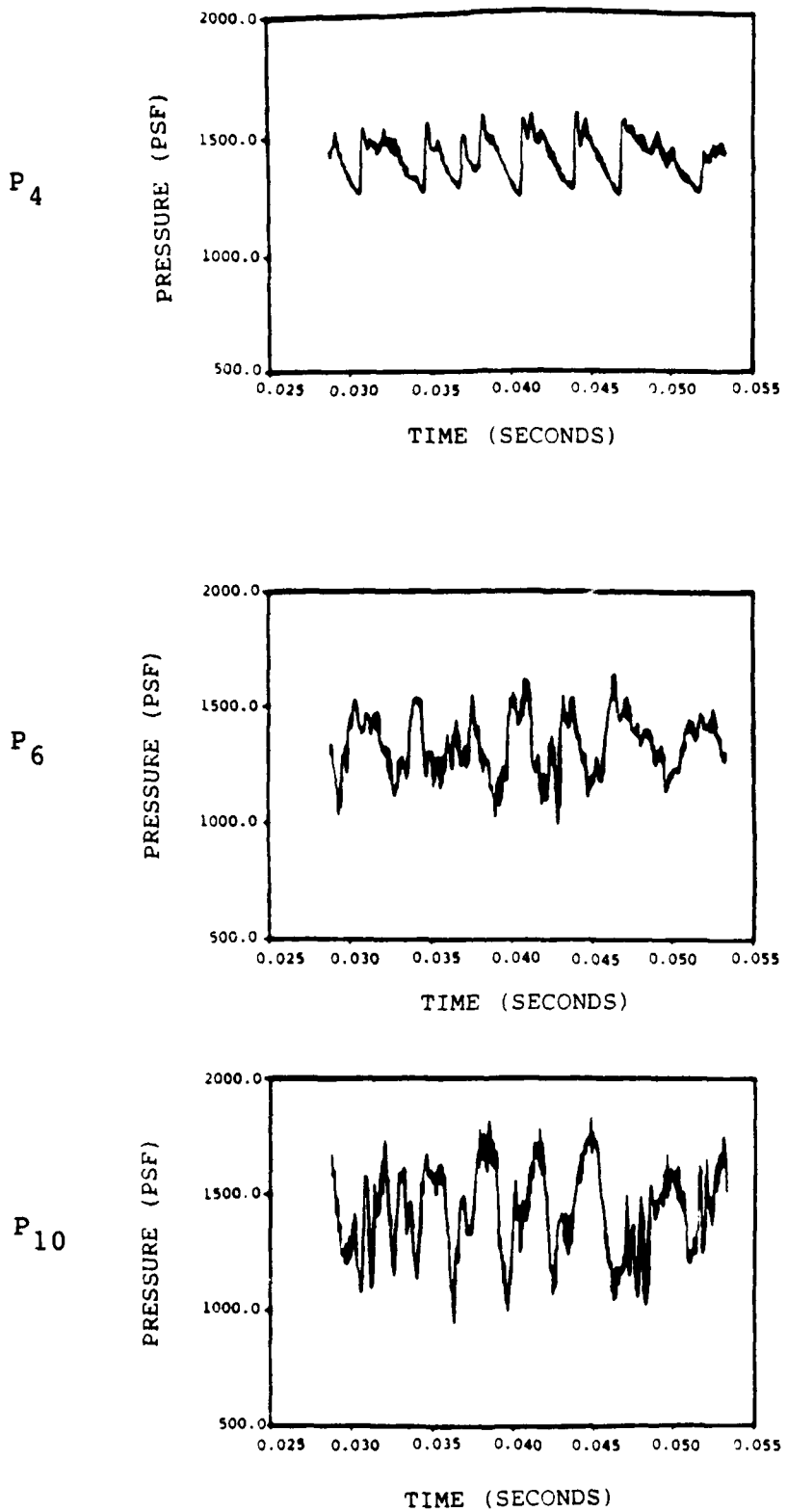

Figure 5. Pressure histograms--fine grid (301 x 41).

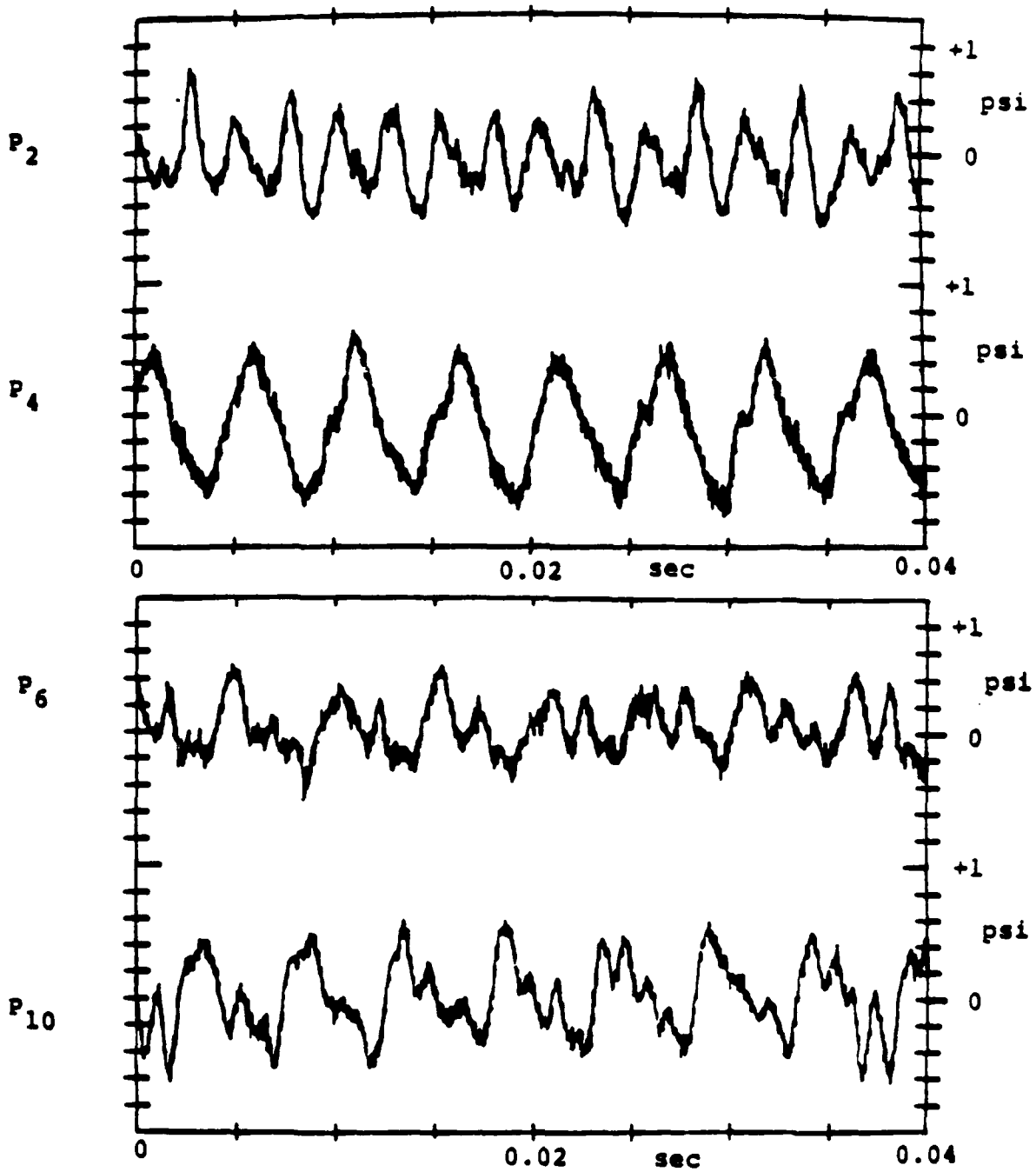

Figure 6. Experimental pressure histograms.

Another benefit of the increased resolution of the medium and fine grids is the ability to better observe the shedding of vorticies generated in the dump region. The shedding phenomena is demonstrated in Figure 7. The time history of the vorticity clearly depicts the unsteady character of the flow and also provides new insight into the flow reattachment phenomena.

In the previous investigation it was noted that for the laminar test cases the computed flowfield did not reattach in the combustor region. The experimental data indicated an average reattachment point near $x = 11.0$ inches. When the computations were done on the medium and fine grids, the reattachment location was in agreement with experiment. Figure 8 displays how the reattachment points move with time. Note that there are several reattachment points at any one time, but the primary reattachment point varies from 8.0 inches to approximately 13.5 inches.

The results of the numerical study were very encouraging. The axial resolution of the computational grid has a dramatic impact on the accuracy of unsteady flow computations. It has been demonstrated that increasing the grid point density in the axial direction leads to better resolution of the large scale vortical structures. This, in turn, leads to increased dissipation and the computed results more closely agree with experiment. However, the accuracy of the computations still could be further improved.

Over the course of the numerical investigation it became apparent that in order to obtain reasonable results the computer code has to be capable of adequately modeling the viscous dissipation. The accuracy of the computed solutions was greatly increased when the grid was refined to allow for resolution of the large scale eddies. It is conjectured that the accuracy of the computer code could be further increased by modeling the fine scale turbulence in the shear layer by application of a "law of the wake" turbulence model. Another

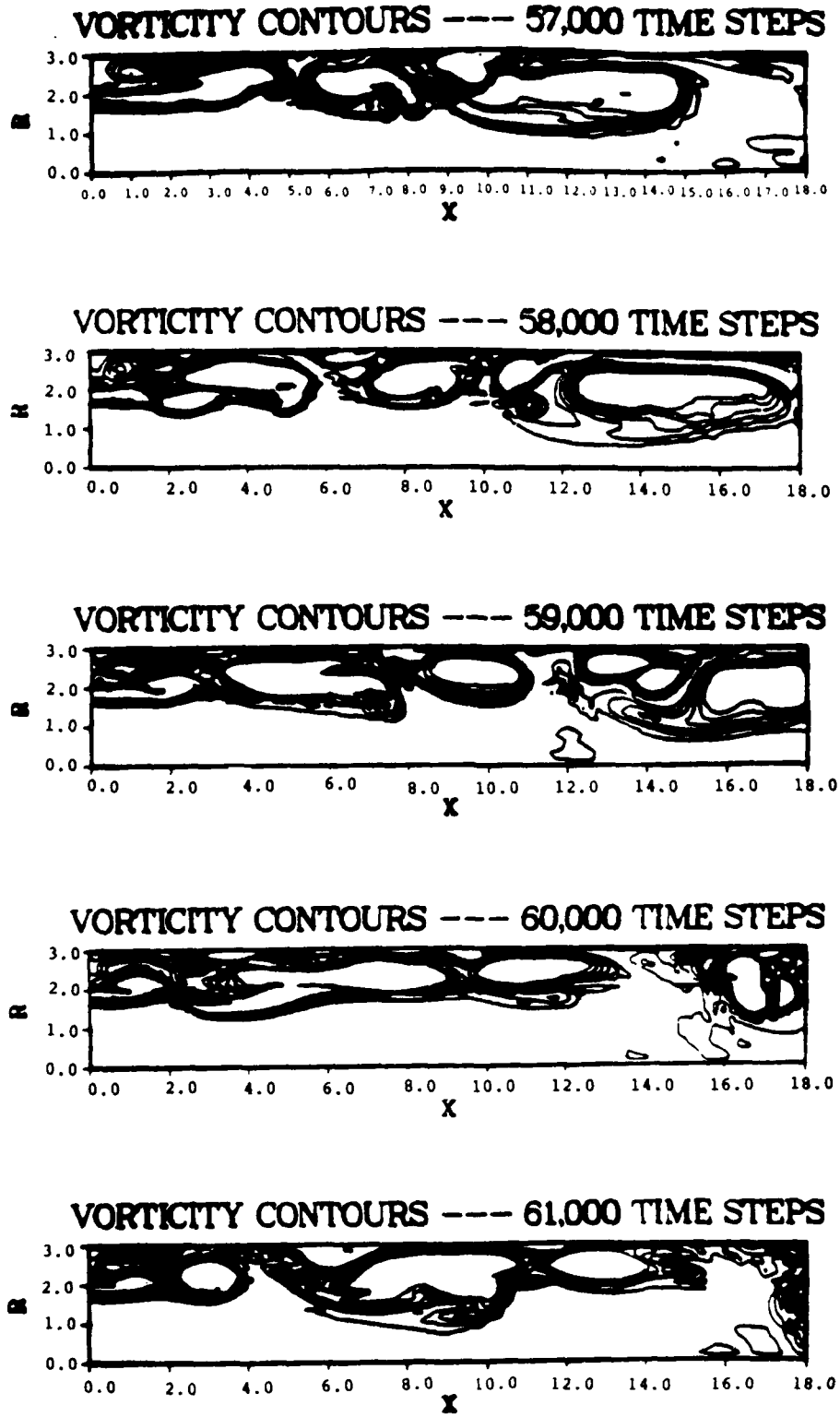

Figure 7. Shedding phenomena.

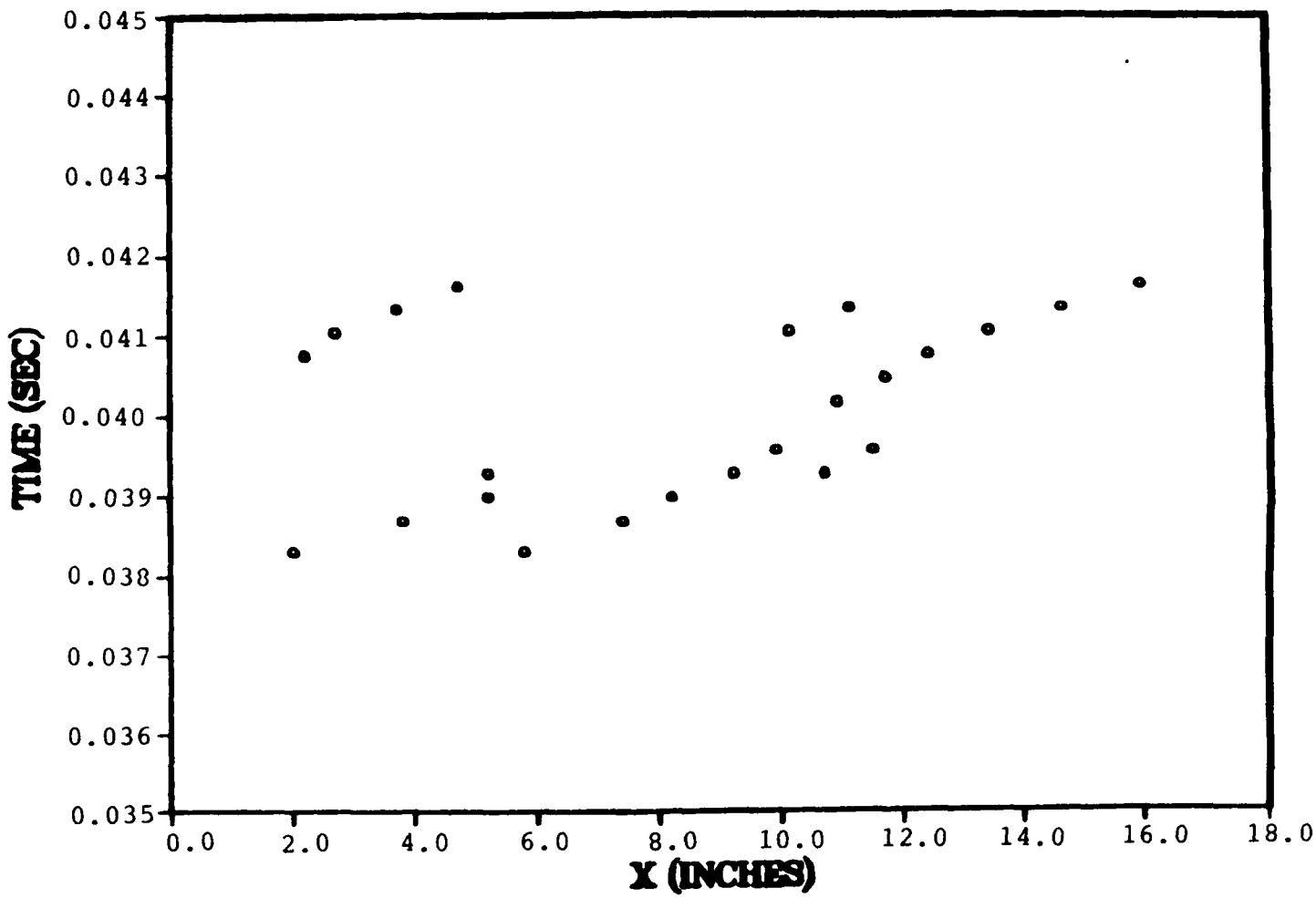

Figure 8. Reattachment phenomenon.

important consideration is the three-dimensional effect. By performing the computations in the three-dimensions instead of assuming an axisymmetric flow, the three-dimensional effect of turbulence may be better simulated.

These results suggest guidelines for the minimum number of grid points necessary for resolving the time-dependent flow features.

2.1.7.2 Quasi-One-Dimensional Model Problem

The quasi-one-dimensional model problem consisted of subsonic deflagration of methane gas and air. The methane-air mixture was heated above the ignition point of the mixture by passing through a normal shock. The numerical model included additional air so the computational fluid represented a 10 percent equivalence ratio of the gas mixture.

2.1.7.2.1 Governing Equations

The chemical formula for the stoichiometric combustion of methane in air is:

$$CH_4 + 2O_2 + 7.52\ N_2 \xrightarrow{K_f} CO_2 + 2H_2O + 7.52\ N_2$$

The governing fluid dynamic equations are:

$$\left| \begin{matrix} \rho A \\ \rho uA \\ \rho E_t A \\ \rho Y_i A \end{matrix} \right|_t + \left| \begin{matrix} \rho uA \\ \{\rho u^2 + P - \tau_{xx}\}A \\ \{u(\rho E_t + P - \tau_{xx}) + \dot{q}_x\}A \\ \{\rho(uY_i - D\frac{dY_i}{dx})\}A \end{matrix} \right|_x = \left| \begin{matrix} 0 \\ \{P - \tau_{xx}\}\frac{dA}{dx} \\ \{-u\tau_{xx} + \dot{q}_x\}\frac{dA}{dx} \\ \dot{m}_i A - \rho D\frac{dY_i}{dx}\frac{dA}{dx} \end{matrix} \right|$$

where

$$E_t = h + \frac{u^2}{2} - \frac{P}{\rho}$$

and

$$h = \sum Y_i\left[\int_{Tref}^{T} CP_i dT + h_f^o\right]$$

The primary difficulties encountered in the integration of Equation (2) is the representation of the mass production terms ($\dot{m}_i$). If a global one-step model is used to calculate the rate of fuel consumption, all other mass production rates are algebraically determined via the law of mass action. Coffee, et al.,[5] developed an expression for fuel consumption. They proposed:

$$\dot{m}_{fuel} = A_1[\rho\ Y_{fuel}]^{\nu_F}\ [\rho\ Y_{oxidizer}]^{\nu_o}\ e\left(-\frac{T_a}{T}\right)$$

where ν_F and ν_o are the stoichiometric coefficients for the global reaction formula. The constants A_1 and T_a are determined from best fit curves generated by a detailed reaction rate model which employs experimental data as input.

2.1.7.2.2 Initial and Boundary Conditions

The incoming flow was supersonic, therefore, all flow variables were specified at station (1), Figure 9. Since the outflow was subsonic, the back pressure $|P_2|$ was specified to ensure the formation of a normal shock in the nozzle.

The incoming flow contained 10 percent of the stoichiometric mass fraction of methane. By a simple analysis, it was determined that only 13 percent of the stoichiometric mass fraction could be burned before thermal choking would occur.

$M_1 = 1.4$

$P_1 = 1000.0$ Psf.

$T_1 = 1350.0$ R

$Y_1 =$ Constant

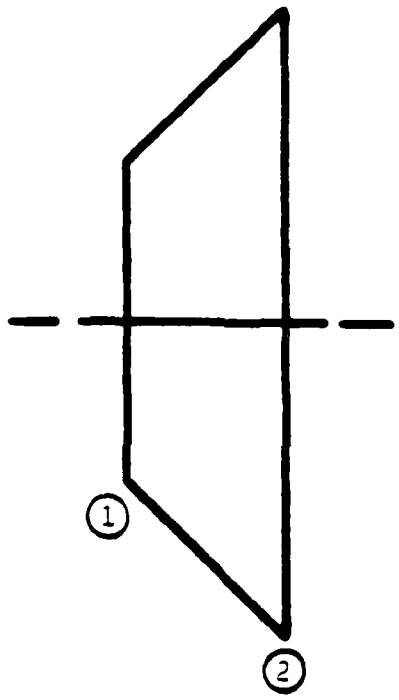

$P_2 = 1805.0$ Psf.

$U_x = T_x = Y_{1,x} = 0.0$

$$\frac{A_2}{A_1} = 3.0$$

Figure 9. Shock Induced Deflagration Model Problem. Quasi-One-Dimensional.

Since nitrogen was the dominant species, the fluid properties were assumed to be those of nitrogen.

$$C_p = \text{Constant} = 5.830 \times 10^3 \ \frac{\text{Lbf - ft}}{\text{slug - R}^\circ}$$

$$k = 2.875 \times 10^{-3} \left\{\frac{T}{491^\circ R}\right\}^{0.94} \frac{\text{Lbf - ft}}{\text{ft - S - R}^\circ}$$

$$D_{N_2,CH_4} = 2.1527 \times 10^{-4} \ \frac{ft^2}{S}$$

$$A_1 = -1.0 \times 10^{18} \left\{\frac{ft^6}{slug^2}\right\} \frac{1}{S}$$

2.1.7.2.3 Results

Figures 10 and 11 depict axial pressure through the nozzle for the reacting and nonreacting cases. The test case shown in Figure 10 incorporated larger amounts of normal stress damping[6] than the nonreacting calculation. The test case shown in Figure 12 has the same amount of normal stress damping as the nonreacting calculation. From the above, it was observed that normal stress damping adequately removes shock induced oscillations without affecting the jump conditions. Figures 13 and 14 depict axial temperature distribution for the reacting and nonreacting cases. The species mass fractions for the reacting case are shown in Figure 15.

The addition of the chemical rate equations did not reduce the stability of the MacCormack algorithm. The time step used was 80 percent of the inviscid CFL limit. This behavior is opposite to that reported by Eklund, et al.,[7] and was primarily due to the global reaction rate model.

2.2 Supersonic Combustion

The second major effort in the computation of ramjet internal flowfields was the investigation of supersonic combustion. For this supersonic flow regime advantage may be taken of an

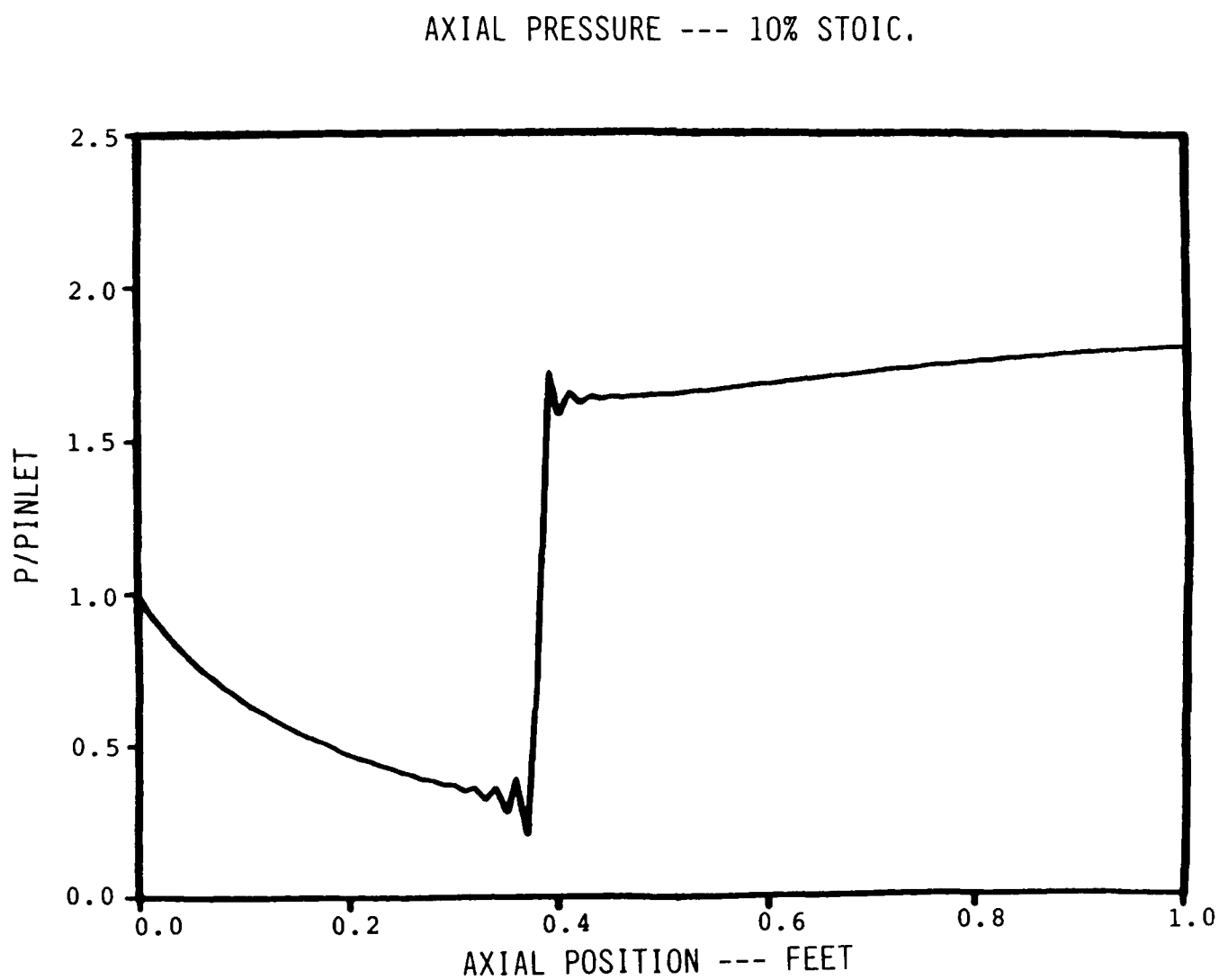

Figure 10. Axial Pressure Profile (Reacting Flow).

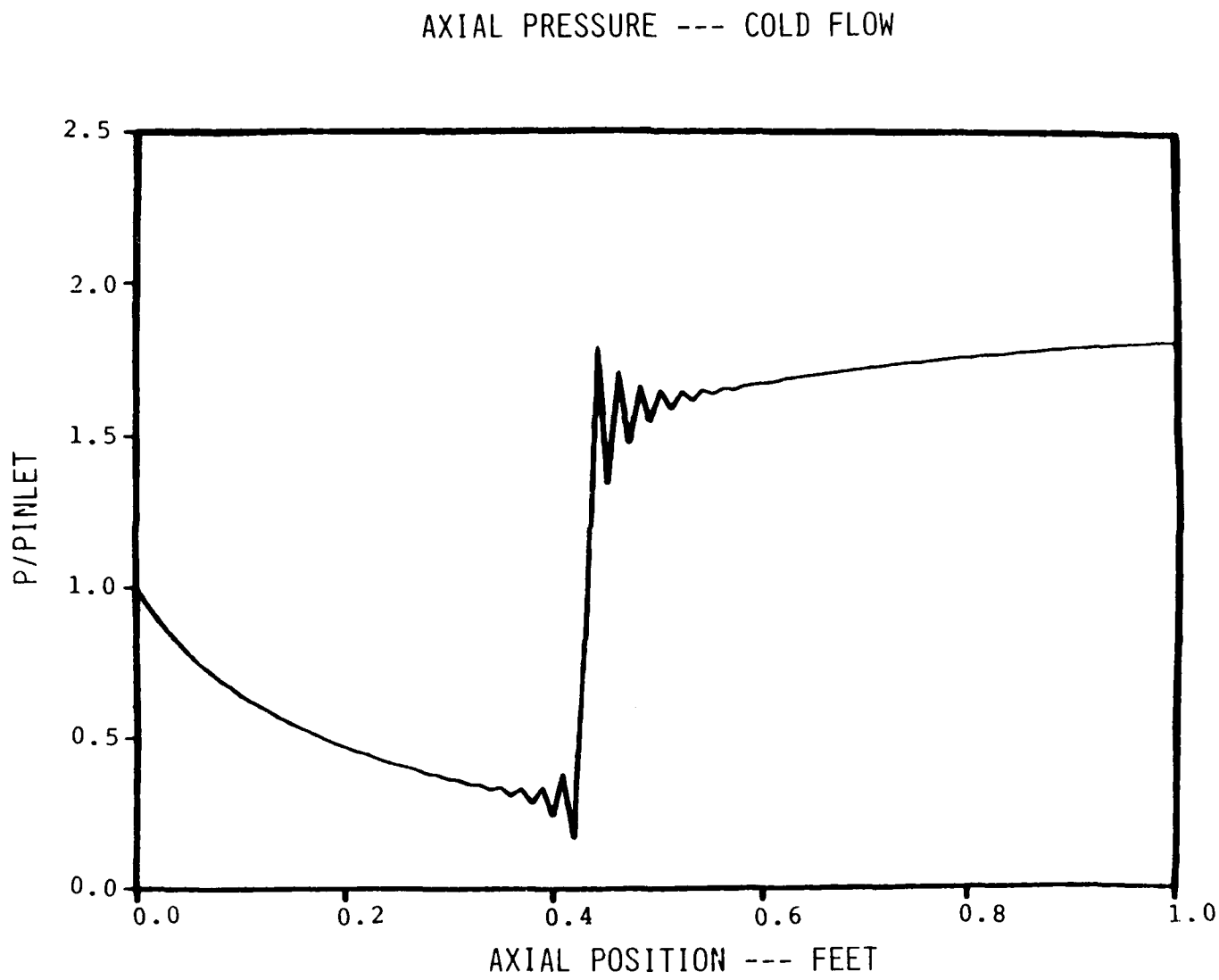

Figure 11. Axial Pressure Profile (Nonreacting Flow).

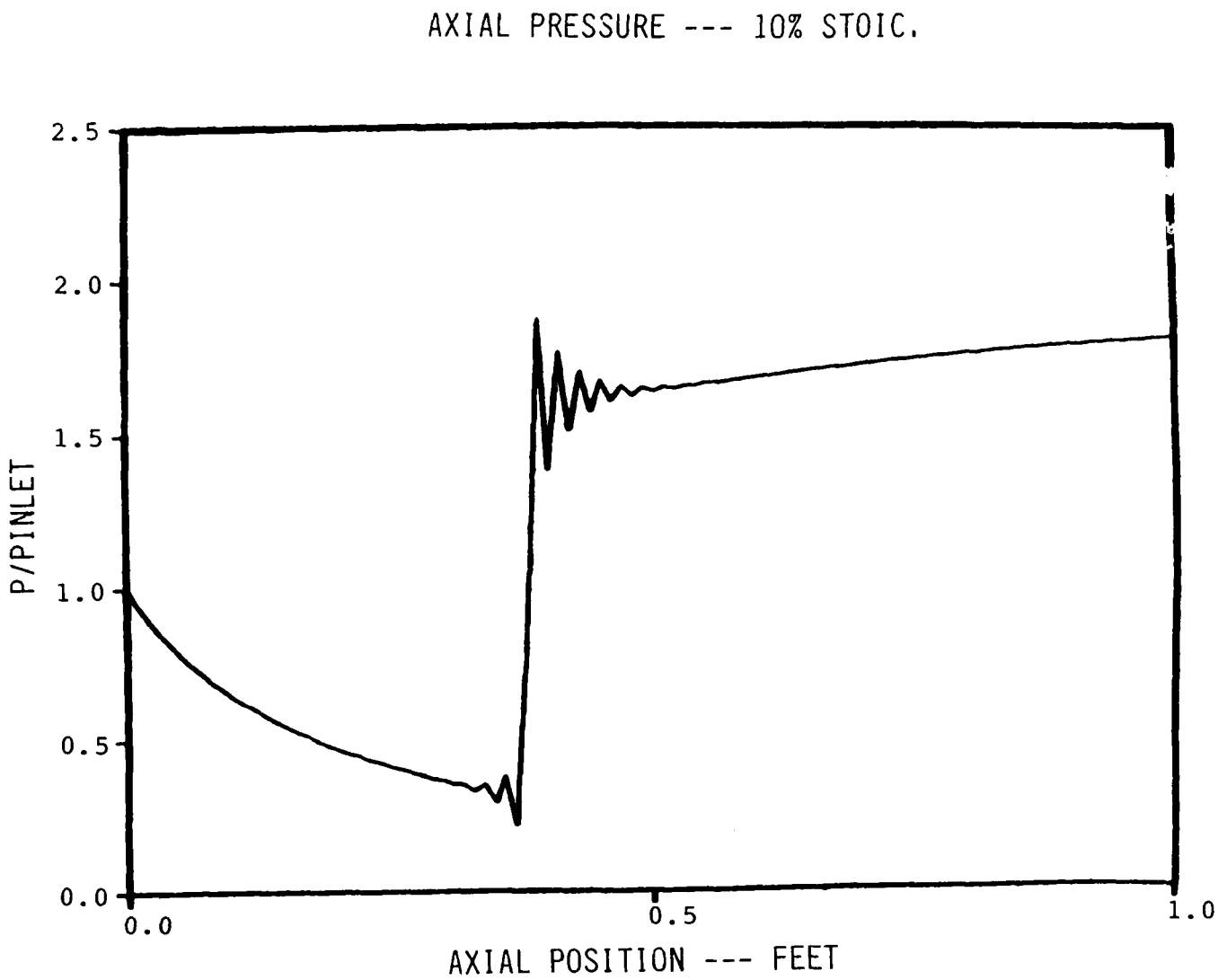

Figure 12. Axial Pressure Profile (Reacting Flow).

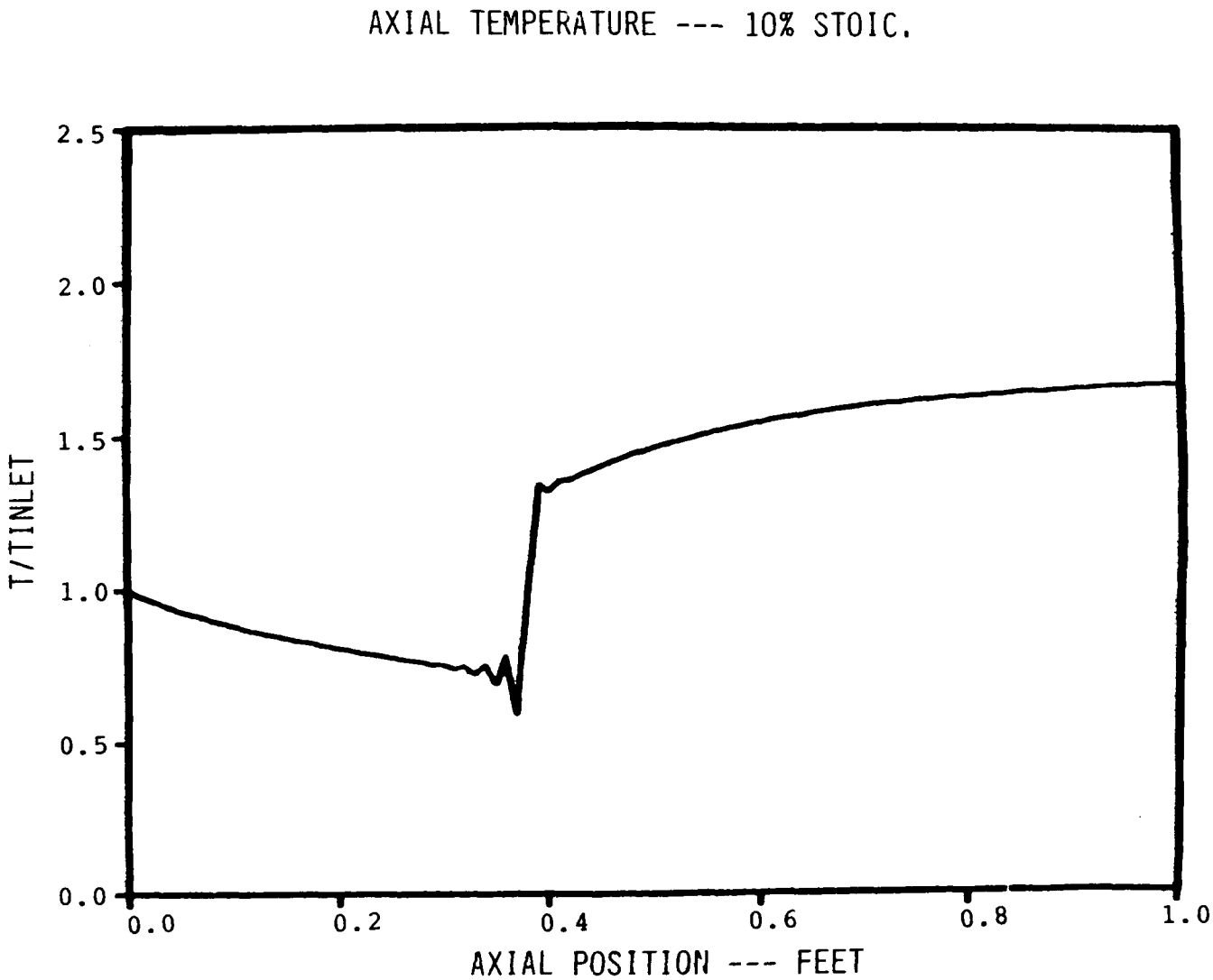

Figure 13. Axial Temperature Profile (Reacting Flow).

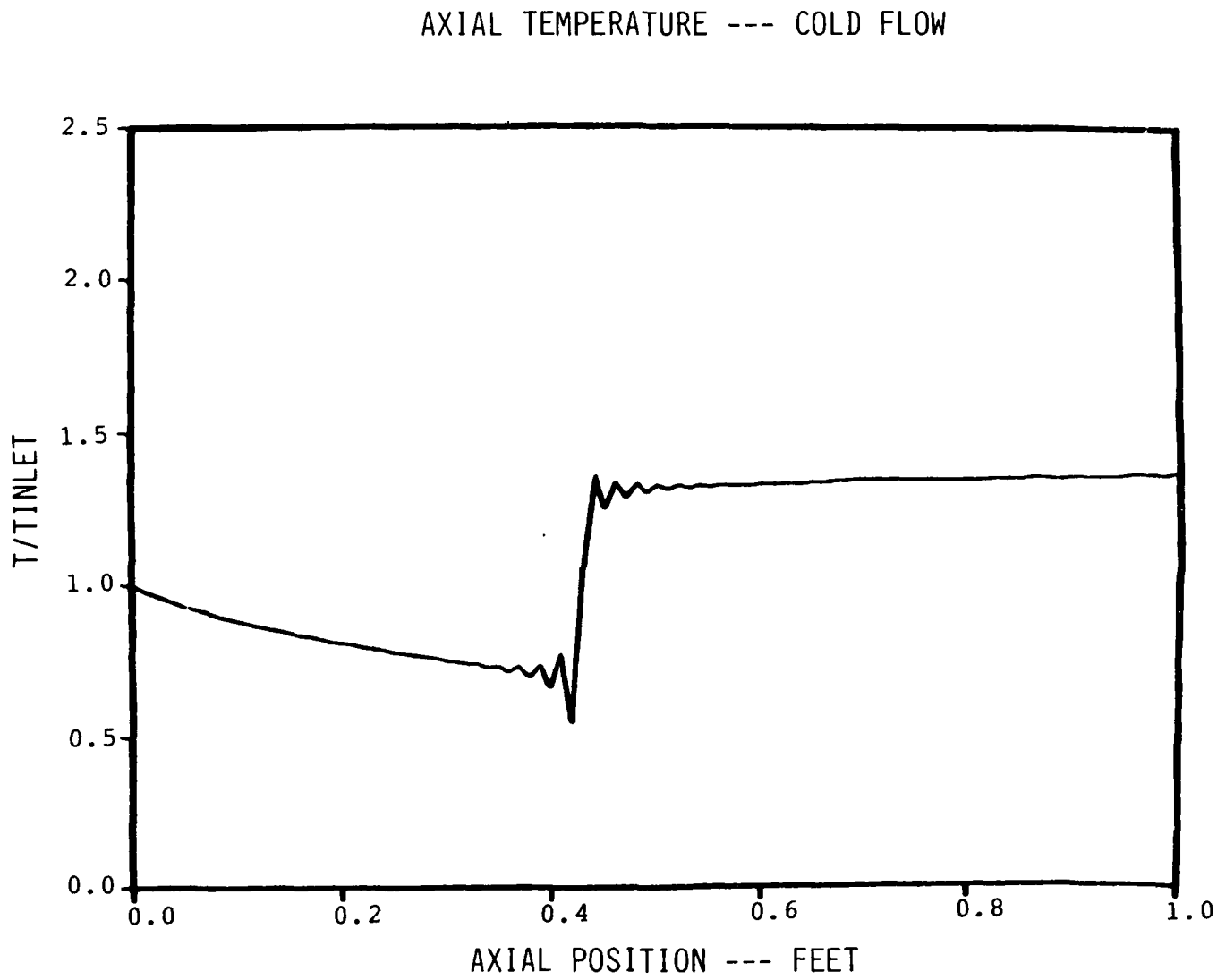

Figure 14. Axial Temperature (Nonreacting Flow).

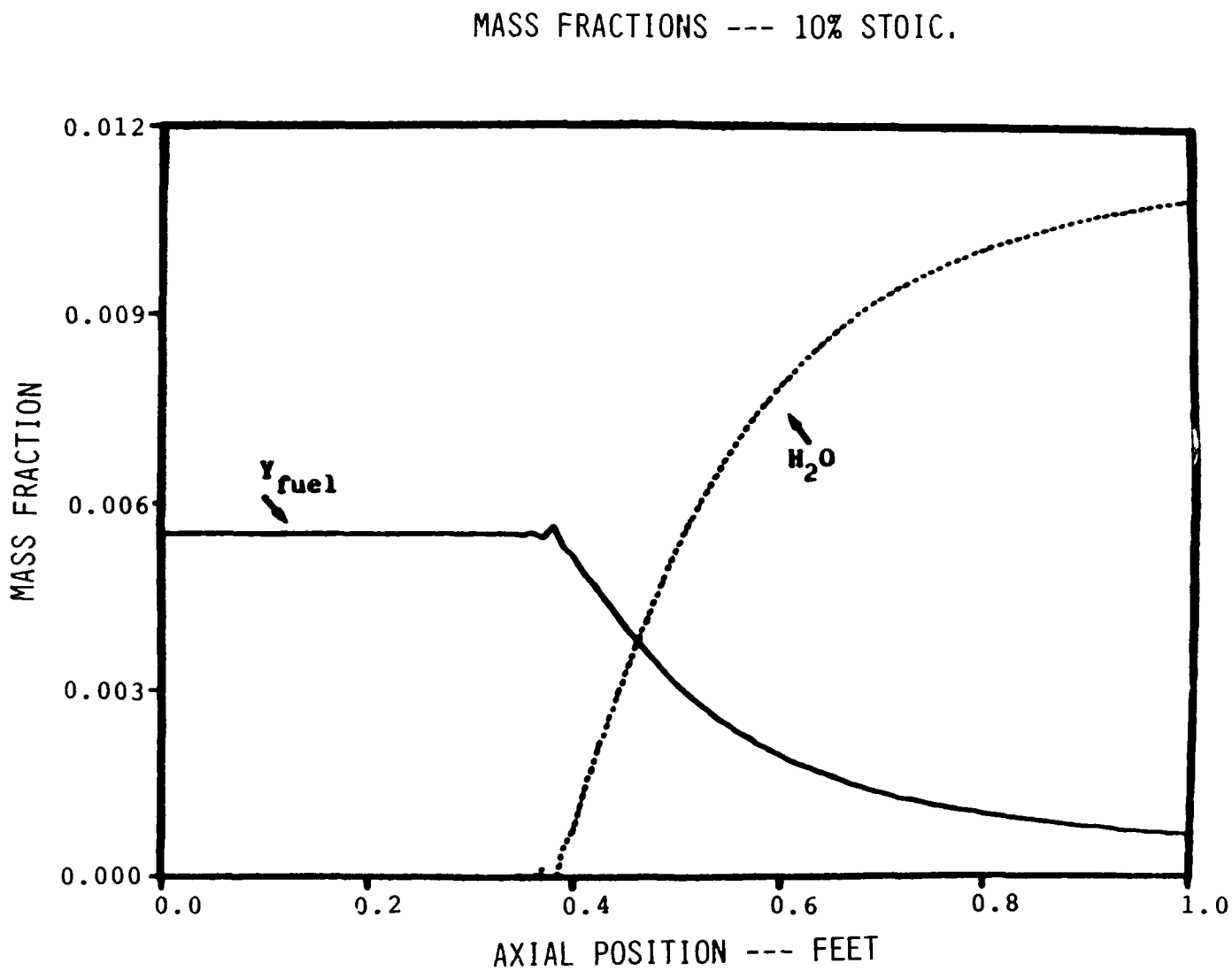

Figure 15. Axial Mass Fractions (Reacting Flow).

approximation which cannot be utilized in subsonic unsteady flows, i.e., PNS. The parabolized Navier-Stokes equations are appropriate for only steady, supersonic, attached flows. This limitation, however, results in at least an order of magnitude reduction in computer time. The savings in computer resources is extremely desirable in systems studies for the Aerospace plane. Therefore, supersonic combustion of hydrogen fuel was examined using the PNS method.

In the following sections the governing equations, boundary conditions, and chemistry for hydrogen/air reaction will be presented. Model problems are solved for several cases to validate the method.

2.2.1 Governing Equations

The steady parabolized Navier-Stokes equations were used in this investigation. In divergence form, the steady Navier-Stokes equations are:

$$E_x + F_y + G_z = H$$

Where the E, F, G, and H vectors are defined as:

$$E = \begin{vmatrix} \rho u \\ \rho u^2 + p - \tau_{xx} \\ \rho uv - \tau_{xy} \\ \rho uw - \tau_{xz} \\ (E_t + p)u - u\tau_{xx} - v\tau_{xy} - w\tau_{xz} - q_x \\ \rho uY_i - \rho DY_{i,x} \end{vmatrix}$$

$$F = \begin{vmatrix} \rho v \\ \rho uv - \tau_{xy} \\ \rho v^2 + p - \tau_{yy} \\ \rho vw - \tau_{yz} \\ (E_t + p)v - u\tau_{xy} - v\tau_{yy} - w\tau_{yz} - q_y \\ \rho vY_i - \rho DY_{i,y} \end{vmatrix}$$

$$G = \begin{vmatrix} \rho w \\ \rho uw - \tau_{xz} \\ \rho vw - \tau_{yz} \\ \rho w^2 + p - \tau_{zz} \\ (E_t + p)w - u\tau_{xz} - v\tau_{yz} - w\tau_{zz} - q_z \\ \rho wY_i - \rho DY_{i,z} \end{vmatrix}$$

$$H = \begin{vmatrix} 0 \\ 0 \\ 0 \\ 0 \\ 0 \\ m_i \end{vmatrix}$$

The governing equations were then transformed from the physical to the computational plane to simplify the numerical integration algorithm. The transformation used in this study was as follows:

$$\zeta = \zeta(x)$$
$$\eta = \eta(x,y,z)$$
$$\zeta = \zeta(x,y,z)$$

Applying the above transformation to the vector equation yields:

$$\{\zeta_x E_\zeta + \eta_x E_\eta + \eta_y F_\eta + \zeta_y F_\zeta + \eta_z G_\eta + \zeta_z G_\zeta\} \frac{1}{J} = \frac{H}{J}$$

where J is the Jacobian of the transformation. The equations are then parabolized in the transformed plane to insure maximum accuracy. In addition, the splitting of the axial streamwise pressure gradient was performed as specified by Vigneron, Rakich, and Tannehill.[8] Performing the parabolization and recasting the above equation into divergence form results in:

$$\left[\frac{\zeta_x E^*}{J}\right]_\zeta + \left[\frac{\eta_x E + \eta_y F + \eta_z G}{J}\right]_\eta + \left[\frac{\zeta_x E + \zeta_y F + \zeta_z G}{J}\right]_\zeta -$$

$$\left\{E^* \left(\frac{\zeta_x}{J}\right)_\zeta + E\left(\frac{\eta_x}{J}\right)_\eta + E\left(\frac{\zeta_x}{J}\right)_\zeta\right\} - \left\{F\left(\frac{\eta_y}{J}\right)_\eta + F\left(\frac{\zeta_y}{J}\right)_\zeta\right\} -$$

$$\left\{G\left(\frac{\eta_z}{J}\right)_\zeta + G\left(\frac{\zeta_z}{J}\right)_\zeta\right\} = -\left(\frac{\zeta_x}{J} P\right)_\zeta + P\left(\frac{\zeta_x}{J}\right)_\zeta + \frac{H}{J}$$

Where the E* and the P vector and the scaler ω are defined as follows (Vigneron, et al.):

$$E^* = \begin{matrix} \rho u \\ \rho u^2 + \omega p \\ \rho uv \\ \rho uw \\ u(E_t + p) \\ u\rho Y_i \end{matrix}$$

$$P = \begin{matrix} 0 \\ (1-\omega)p \\ 0 \\ 0 \\ 0 \end{matrix}$$

$$\omega = \frac{\gamma M_x^{\ 2}}{(1+(\gamma-1)M^2)}$$

The above equations contain the geometric conservation law (GCL) terms (Thomas and Lombard[9]) and the metric

derivatives which result from returning to the conservation law form in the transformed plane. It was found that the GCL terms must be included into the formulation in order to eliminate source term-like errors (Gielda and McRae[10,11]).

Applying the transformation and parabolization to the viscous stress and heat flux terms yields the following relations:

$$\tau_{xx} = \frac{2\mu}{3}\{2(u_\eta\eta_x + u_\zeta\zeta_x) - (v_\eta\eta_y + v_\zeta\zeta_y + w_\eta\eta_z + w_\zeta\zeta_z)\}$$

$$\tau_{yy} = \frac{2\mu}{3}\{2(v_\eta\eta_y + v_\zeta\zeta_y) - (u_\eta\eta_x + u_\zeta\zeta_x + w_\eta\eta_z + w_\zeta\zeta_z)\}$$

$$\tau_{zz} = \frac{2\mu}{3}\{2(w_\eta\eta_z + w_\zeta\zeta_z) - (v_\eta\eta_y + v_\zeta\zeta_y + u_\eta\eta_x + u_\zeta\zeta_x)\}$$

$$\tau_{xy} = \mu\{u_\eta\eta_y + u_\zeta\zeta_y + v_\eta\eta_x + v_\zeta\zeta_x\}$$

$$\tau_{yz} = \mu\{w_\eta\eta_y + w_\zeta\zeta_y + v_\eta\eta_z + v_\zeta\zeta_z\}$$

$$\tau_{xz} = \mu\{u_\eta\eta_z + u_\zeta\zeta_z + w_\eta\eta_x + w_\zeta\zeta_x\}$$

and

$$\dot{q}_x = \frac{C_p\mu}{Pr}\{T_\eta\eta_x + T_\zeta\zeta_x\} + \rho D\,\Sigma h_i(Y_{i,\eta}\eta_x + Y_{i,\zeta}\zeta_x)$$

$$\dot{q}_y = \frac{C_p\mu}{Pr}\{T_\eta\eta_y + T_\zeta\zeta_x\} + \rho D\,\Sigma h_i(Y_{i,\eta}\eta_x + Y_{i,\zeta}\zeta_x)$$

$$\dot{q}_z = \frac{C_p\mu}{Pr}\{T_\eta\eta_z + T_\zeta\zeta_z\} + \rho D\,\Sigma h_i(Y_{i,\eta}\eta_z + Y_{i,\zeta}\zeta_z)$$

These relations were then used in the formulation of the E, F, and G vectors. The thermodynamic properties (C_p, R, etc.) were functions of species mass fraction and the local static temperature. C_p was determined from the local mass fraction and C_{pi} were calculated via curve fits with ranges of applicability up to 6500°R.

2.2.2 Numerical Method

MacCormack's[12] well-known predictor-corrector scheme was used to integrate the governing equations. The application of this numerical integration scheme is well-documented in References 10 and 11, and, therefore, will not be repeated.

The metrics in the previous equations were calculated by second order central differences except for the ζ derivatives which were calculated by first order backward differences. First order backward differences for the ζ derivatives were required since only two planes of data are stored in computer memory for each marching step. After each marching step the current information at the n+1 level is shifted to the nth level.

The viscous and heat flux terms used in forming the E, F, and G vectors were differenced in the opposite direction from the flux derivative. For example, in forming

$$\{E\eta_x + F\eta_y + G\eta_z\}\ 1/J$$

in the predictor step, the derivatives with respect to η were calculated by one-sided backward differences, while central differencing was used for the ζ derivatives. This must be done to maintain the three-point stencil for the viscous terms. Likewise, in forming

$$\{E\zeta_x + F\zeta_y + G\zeta_z\}\ 1/J$$

in the predictor step, the ζ derivatives were calculated via one-sided backward differences and the η derivatives were calculated by central differences. In the corrector sweep the one-sided differences switch from backward to forward.

Streamwise Pressure Gradient

As stated in the section on governing equations, the streamwise pressure gradient is split in a manner identical to that proposed by Vigneron, et al. Vigneron has proved that a fraction of the streamwise pressure gradient can be included in the governing equations and still maintain algorithm stability while marching

through regions of locally subsonic flow. Recalling the pressure splitting scheme, where E* and the P vector are defined as:

$$E^* = \begin{vmatrix} \rho u \\ \rho u^2 + \omega p \\ \rho uv \\ \rho uw \\ (E_t + p)u \\ \rho u Y_i \end{vmatrix} \qquad P = \begin{vmatrix} 0 \\ (1-\omega)p \\ 0 \\ 0 \\ 0 \\ 0 \end{vmatrix}$$

The function ω is the maximum allowable fraction of the streamwise pressure gradient which can be retained and maintain stable marching. Taking into account the nonlinear effects of the governing equations, ω is redefined as:

$$\omega = \frac{\sigma \gamma M^2_x}{1+(\gamma-1)M^2_x}$$

The value of the safety factor σ was approximately 0.75.

The major benefit of the Vigneron technique is its effect on the decoding of the axial flux vector E*. A quadratic equation for u velocity component results when the dependent variables are computed from the components of the E* or E* vectors. The roots of the quadratic equation correspond to either the subsonic or supersonic solution (elliptic or hyperbolic character of the governing equation). By incorporating the Vigneron scheme, the character of the governing equations remains hyperbolic throughout the flowfield. Therefore, only the root corresponding to the hyperbolic solution is used.

2.2.3 Initial and Boundary Conditions

The initialization of a PNS code requires an initial starting solution. The PNS solution is then marched downstream from this initial data plane. During the investigation two types of initial conditions were employed: (1) The initial data plane was set equal to free stream conditions or the

conditions upstream of the inlet. (2) The initial data plane was generated by another integration scheme (i.e., a time dependent FNS solution). The latter technique is most beneficial when regions of streamwise separation are encountered.

At all solid surfaces, isothermal and no-slip boundary conditions were applied. The pressure and species mass fractions were determined from zero dp/dn and zero dY_i/dn boundary conditions respectively.

2.2.4 Numerical Smoothing

The MacCormack explicit algorithm is second order accurate in the marching as well as the transverse and normal coordinate direction. Since the algorithm is second order accurate, the leading term is third order or dispersive. The MacCormack explicit PNS code incorporated both normal stress damping (McRae[6]) and modified MacCormack[13] second order smoothing (Gielda and McRae[10,11]). Figures 16 and 17 depict the surface pressure on a secant-ogive-cylinder projectile at Mach 4 and angle of attack, without and with normal stress damping. The oscillations associated with the program start-up are observed to be suppressed immediately with no offset in surface pressure. This form of damping results when the normal stress terms are modified as shown below.

The normal stress terms (τ_{xx}, τ_{yy}, and τ_{zz}) are defined as:

$$\tau_{xx} = \mu(2u_x) + \sigma_\eta$$

where σ_η is normally defined as:

$$\sigma_\eta = -\frac{2}{3}\mu(\nabla\cdot\bar{V})$$

Normal stress damping results when σ_η is multiplied by a factor β, where β is of the form:

$$\beta = (1-\mathrm{DNS1}\,\frac{p_w}{p_\infty} - \mathrm{DNS2}\,\frac{p}{p_\infty})$$

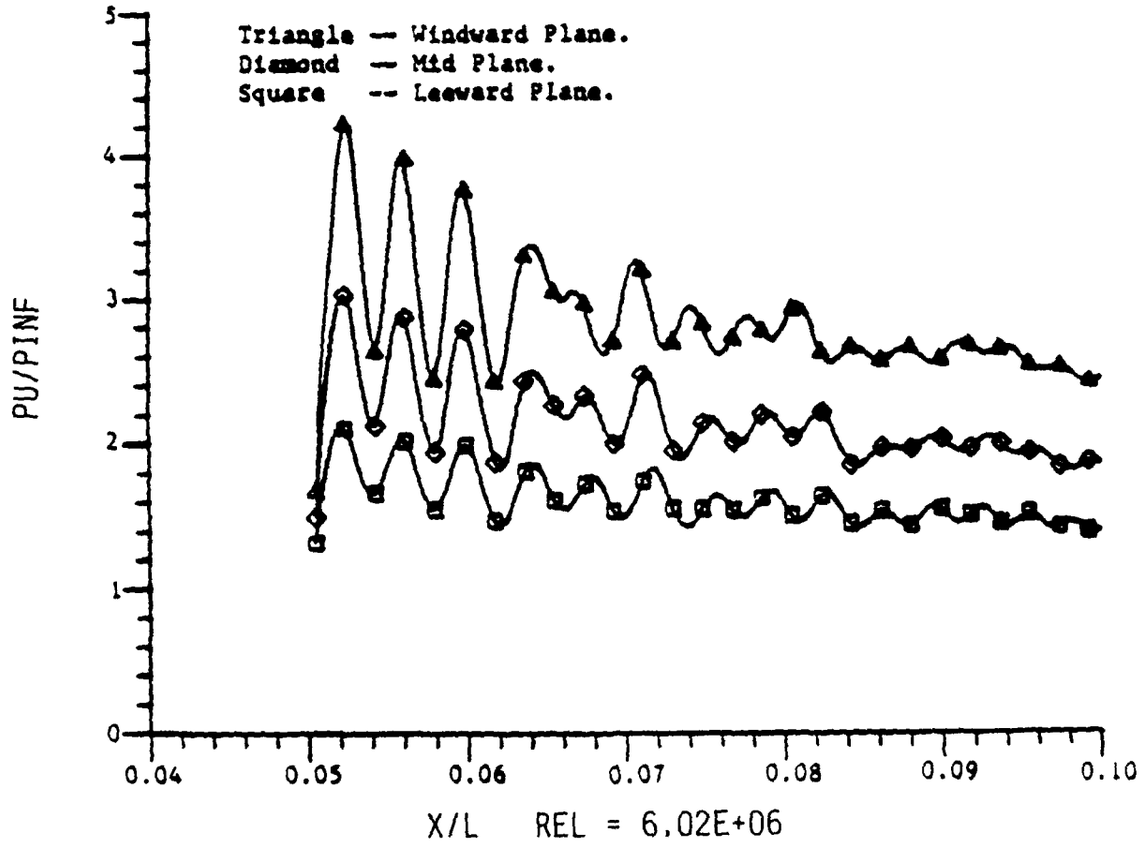

Figure 16. Computed surface pressure on a secant-ogive-cylinder-boat-tail projectile at 4.0 degrees angle of attack without normal stress damping (M_∞=4.0).

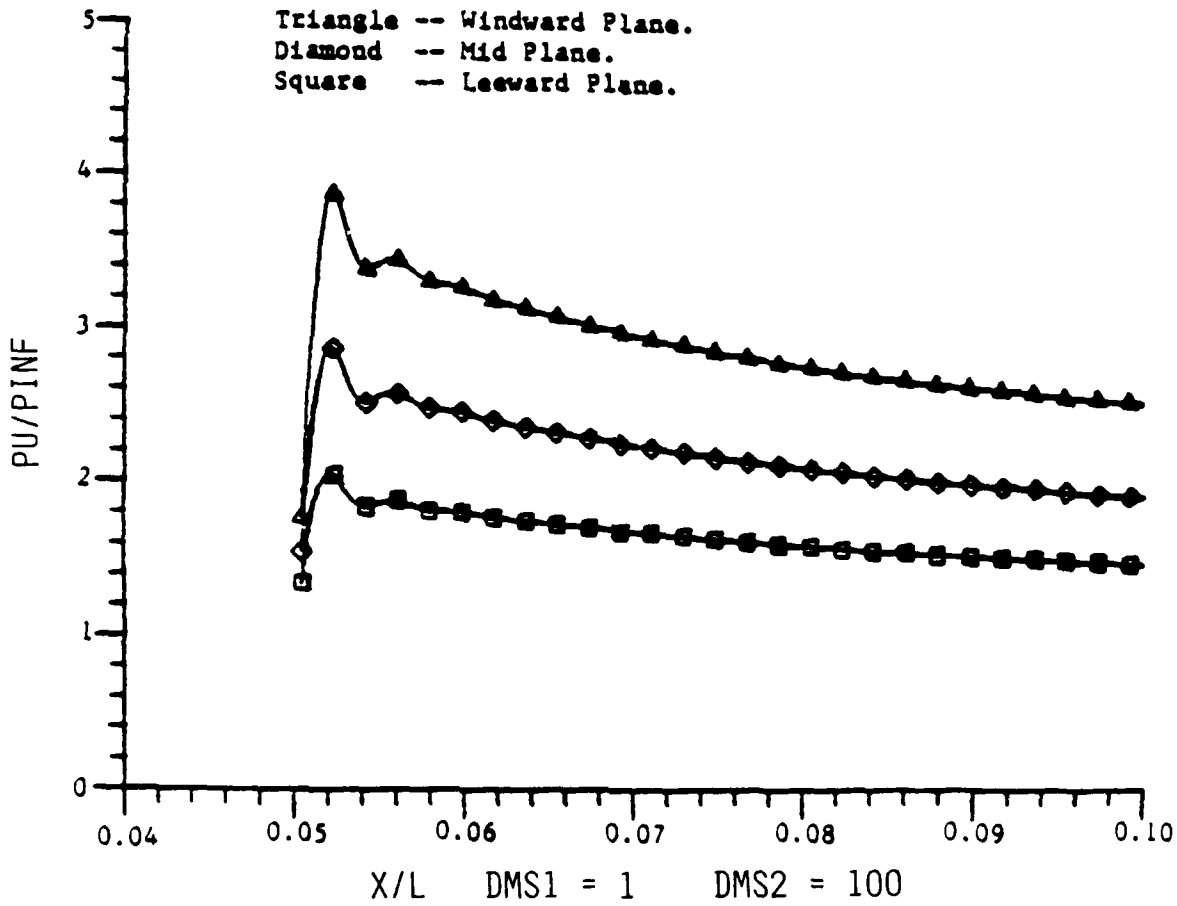

Figure 17. Computed surface pressure on a secant-ogive-cylinder-boat-tail projectile at 4.0 degrees angle of attack with normal stress damping (M_∞=4.0).

The typical values of DNS1 and DNS2 varied from 0<DNS1<10 and 0<DNS2<10.

In addition to normal stress damping, second order smoothing was also used. The functional form of this damping was:

$$\text{Damping} = (A1(j,k)E(j,k,n)^*_{\eta\eta} + A2(j,k)E(j,k,n)^*_{\zeta\zeta}) \left[\frac{\zeta_x}{J}\right]$$

Where A1 and A2 are defined by:

$$A1(j,k) = CDY\ ABS \left\{\frac{p_{\eta\eta}}{p(j+1,k)+2p(j,k)+p(j-1,k)}\right\}$$

$$A2(j,k) = CDZ\ ABS \left\{\frac{p_{\zeta\zeta}}{p(j,k+1)+2p(j,k)+p(j,k-1)}\right\}$$

The second order explicit damping was applied in both the predictor and corrector steps. In the predictor the damping was based on E^{*n}, while in the corrector the damping was based on E^{*n+1}. The values of CDY and CDZ varied from 0.0 to 0.05. The second order damping was used sparingly and primarily during program initiation.

Once the initial starting transients were eliminated the normal stress and second order damping were removed. Typically this was accomplished by reducing the coefficients DNS1, DNS2, CDY, and CDZ by 0.5 percent per marching step.

2.2.5 Reaction Rate Modeling

Hydrogen-oxygen reaction has been thoroughly investigated. Twelve species and 25 reactions have been identified and are listed in Table 6.[14] A simpler 8-reaction system is also identified in the Table. However, to begin the investigation a single global reaction was explored.

For the preliminary supersonic/hypersonic combustion computations global chemical reaction rates were employed. The global reaction rate models were incorporated in an

effort to reduce computational and storage requirements. Even though the global models do not predict accurate flame structure, they do perform adequately in computing the jump conditions across the flame. The global reaction for the stoichiometric combustion of hydrogen in air is given by:

$$2H_2 + O_2 + 3.76N_2 \longrightarrow 2H_2O + 3.76N_2$$

The global reaction rate Varma, Chatwani, and Bracco[15] was used in this investigation. In addition to the finite rate model, an additional reaction rate model based on chemical equilibrium (Varma, et al.) was considered.

The equilibrium reaction rate models are well-suited for high temperature flames encountered in hydrogen combustion. These models allow for forward and backward reaction rates. Unfortunately, the equilibrium models are not well-suited for vector processing computers since they require frequent table "look-up" operations.

2.2.6 Finite Rate Model

As stated above, the global reaction rate model of Varma, et al., was considered. The global finite rate equation is written as:

$$m_{fuel} = -A_1[H_2]^{1.1}[O_2]^{1.1}e^{\left(-T_a/T\right)}M_w(H_2)$$

The quantities in the brackets represent the local concentration of the species. $M_w(H_2)$ is the molecular weight of hydrogen. The activation temperature, T_a, and the pre-exponential constant A_1 were found to be strong functions of the equivalence ratio of the mixture.[15]

2.2.7 Equilibrium Reaction Rate Modeling

The primary limitation of the finite rate chemistry models are that they are defined by a single Arrhenius type reaction. However, in regions of high temperature these models do not perform as well since there are significant shifts in

TABLE 6 SPECIES AND REACTIONS[a]

Species

1	H	7	N_2
2	O	8	N
3	H_2O	9	NO
4	OH	10	NO_2
5	O_2	11	HO_2
6	H_2	12	HNO_2

Reactions

1	$HNO_2 + H - NO + OH + H$	14	$OH + OH - H + HO_2$
2	$NO_2 + H - NO + O + H$	15	$H_2O + O - H + HO_2$
*3	$H_2 + H - H + H + H$	16	$OH + O_2 - O + HO_2$
*4	$O_2 + H - O + O + H$	17	$H_2O + O_2 - OH + HO_2$
*5	$H_2O + H - OH + H + H$	18	$H_2O + OH - H_2 + HO_2$
*6	$OH + H - O + H + H$	19	$O + N_2 - N + NO$
7	$HO_2 + H - H + O_2 + H$	20	$H + NO - N + OH$
*8	$H_2O + O - OH + OH$	21	$O + NO - N + O_2$
*9	$H_2O + H - OH + H_2$	22	$NO + OH - H + NO_2$
*10	$O_2 + H - OH + O$	23	$NO + O_2 - O + NO_2$
*11	$H_2 + O - OH + H$	24	$NO_2 + H_2 - H + HNO_2$
12	$H_2 + O_2 - OH + OH$	25	$NO_2 + OH - NO + HO_2$
13	$H_2 + O_2 - H + HO_2$		

Reaction Rates

	Forward Rate Constant[b]			Reverse Rate Constant[b]		
	A	B	C	A	B	C
1	5.0×10^{17}	-1.0	25000	8.0×10^{15}	0	-1000
2	1.1×10^{16}	0	32712	1.1×10^{15}	0	-941
3	5.5×10^{18}	-1.0	51987	1.8×10^{18}	-1.0	0
4	7.2×10^{18}	-1.0	59340	4.0×10^{17}	-1.0	0
5	5.2×10^{21}	-1.5	59386	4.4×10^{20}	-1.5	0
6	8.5×10^{18}	-1.0	50830	7.1×10^{18}	-1.0	0
7	1.7×10^{16}	0	23100	1.1×10^{16}	0	-440
8	5.8×10^{13}	0	9059	5.3×10^{12}	0	503
9	8.4×10^{13}	0	10116	2.0×10^{13}	0	2600
10	2.2×10^{14}	0	8455	1.5×10^{13}	0	0
11	7.5×10^{13}	0	5586	3.0×10^{13}	0	4429
12	1.7×10^{13}	0	24232	5.7×10^{11}	0	14922
13	1.9×10^{13}	0	24100	1.3×10^{13}	0	0
14	1.7×10^{11}	0.5	21137	6.0×10^{13}	0	0
15	5.8×10^{11}	0.5	28686	3.0×10^{13}	0	0
16	3.7×10^{11}	0.64	27840	1.0×10^{13}	0	0
17	2.0×10^{12}	0.5	36296	1.2×10^{13}	0	0
18	1.2×10^{12}	0.21	39815	1.7×10^{13}	0	12582
19	5.0×10^{13}	0	37940	1.1×10^{13}	0	0
20	1.7×10^{14}	0	24500	4.5×10^{13}	0	0
21	2.4×10^{11}	0.5	19200	1.0×10^{12}	0.5	3120
22	2.0×10^{11}	0.5	15500	3.5×10^{14}	0	740
23	1.0×10^{12}	0	22800	1.0×10^{13}	0	302
24	2.4×10^{13}	0	14500	5.0×10^{11}	0.5	1500
25	1.0×10^{11}	0.5	6000	3.0×10^{12}	0.5	1200

[a]The first 7 species and the starred reactions constitute the 8-reaction system.

[b]Form of rate constant is $k = AT^{B}\exp(-C/T)$ with k in cm^3/mole-sec or $cm^6/mole^2$-sec.

chemical equilibrium. In order to improve on the accuracy of the finite rate models, the equilibrium reaction rate of Varma was incorporated into a version of the PNS code (SSCPNSEQ) modified to perform calculations with equilibrium chemistry in a zone of supersonic combustion.

The global chemical reaction equation employing the equilibrium reaction rate model is written as:

$$2H_2 + O_2 + 3.76N_2 \underset{kb}{\overset{k_f}{\rightleftharpoons}} 2H_2O + 3.76N_2$$

The rate of production/depletion of species j is defined by:

$$[C_j] = \{[C_j] - [C^*]\}/\tau$$

where $[C_j]$ is the local concentration of species j and $[C^*_j]$ is the concentration of species j if the mixture were in chemical equilibrium. τ is defined as the characteristic time of the global reaction and is given by:

$$1/\tau = B[H_2]^{0.6}[O_2]^{0.6}\ e^{\left(-T_a/T\right)}$$

As in the case of the finite rate models the constants T_a and B are functions of the equivalence ratio of the mixture. For complete details see Reference 15.

2.2.8 Equilibrium Chemistry

To devise a combustion model it is necessary to examine the equilibrium state at the final condition. To accomplish this task nine species are included. At the temperature levels involved 3 species may be eliminated from the 12 variables listed in Table 6 (i.e., NO_2, HO_2, and HNO_2).

The procedure is similar to the approach taken in Section 2.2.6. The mole fractions of the equilibrium composition of the products of combustion of H_2 are determined using the equations involving the equilibrium constants with the assumption that the component gases obey the equation of state for an ideal gas.

$$P_i = \frac{\rho_i RT}{M_i}$$

The general chemical reaction of the nine species may be written as follows:

$$H_2 + \frac{0.5}{\phi}(O_2 + 3.76N_2) \rightarrow n_{N_2}(N_2) + n_{O_2}(O_2) + n_{H_2O}(H_2O)$$

$$+ n_{NO}(NO) + n_{OH}(OH) + n_H(H) + n_O(O) + n_N(N) + n_{H_2}(H_2)$$

where n_i = the number of moles of product "i"
ϕ = equivalence ratio

Three elements are involved (H,O,N) and, hence, three conservation of chemical species equations may be specified.

$$H: \quad 2 = n_{N_{H_2O}} + n_{OH} + n_H \; 2n_{H_2}$$

$$O: \quad 2\left[\frac{0.5}{\phi}\right] = 2n_{O_2} + n_{H_2O} + n_{NO} + n_{OH} + n_O$$

$$N: \quad 2\left[\frac{0.5}{\phi}\right] 3.76 = 2n_{N_2} + n_{NO} + n_N$$

Since there are nine unknown molar species values, six equilibrium constants are required to close the system.

$$K_{H_2O} = \frac{n_{H_2O}}{\sqrt{n_{H_2}}\sqrt{n_{O_2}}} = K_{p,H_2O}\sqrt{\frac{p}{n}}$$

$$K_{NO} = \frac{n_{NO}}{\sqrt{n_{N_2}}\sqrt{n_{O_2}}} = K_{p,NO}$$

$$K_N = \frac{n_N}{\sqrt{n_{N_2}}} = K_{p,N}\sqrt{\frac{n}{p}}$$

$$K_O = \frac{n_O}{\sqrt{n_{O_2}}} = K_{p,O}\sqrt{\frac{n}{p}}$$

$$K_{OH} = \frac{n_{OH}}{\sqrt{n_{H_2}}\sqrt{n_{O_2}}} = K_{p,OH}$$

$$K_H = \frac{n_H}{\sqrt{n_{H_2}}} = K_{p,H}\sqrt{\frac{n}{p}}$$

where $K_{p,i} = f(t)$ from JANNAF Tables. Two additional variables appear in these equations, i.e., p and n.

$p = \Sigma p_i$ = specified pressure

$n = \Sigma n_i$ = total number of moles of the combustion products which becomes an auxiliary equation.

The problem is now formulated. Given ϕ, p, and T there exist 10 algebraic equations involving 9 molar values (n_i) plus the value for the total number of moles (n). Conceptually, this system of equations could be reduced to a single high degree polynomial. Physical reasoning requires that only one positive real root exist. However, in place of reducing the system to one single equation, in practice the entire system of equations is solved by iteration.

An example problem has been solved for ϕ=1 and p=1 atmosphere, over the temperature range of interest. These conditions are typical of the scramjet combustor state and serve to identify the dominant species. A summary of the results are shown in the following table.

2.2.9 Heats of Formation

Once the equilibrium state has been identified the overall heat release during combustion may be computed from the heats of formation of the individual species.

$$\Delta h_c = \Sigma n_i \Delta H_f^\circ$$

The following heat of combustion values were determined using information from Tables 7 and 8 and JANNAF values for ΔH_f°.

T (°R)	Δh_c (kcal/mole)
3600	-59.5
4500	-53.7
5400	-27.4
6300	+40.6

From these results it is apparent that combustion temperatures must be limited to values below 5000°R in order to maintain useful values for the heat of combustion (Figure 18).

2.2.10 Model Problems for Supersonic Combustion

During this investigation two model problems were computed. In order to accomplish this task the computed solutions were compared to experimental data and the computations of others.

The validation test cases consisted of: (1) Laminar, two-dimensional hypersonic flow over a 15 degree compression ramp. (2) Turbulent, two-dimensional supersonic combustion of hydrogen in vitiated air.

TABLE 7
HYDROGEN-AIR COMBUSTION

ϕ=1 Equilibrium States p=1 Atmosphere

T	3600°R	4500°R	5400°R	6300°R
K_{H_2O}	$3467\sqrt{\frac{p}{n}}$	$167\sqrt{\frac{p}{n}}$	$22.0\sqrt{\frac{p}{n}}$	$5.15\sqrt{\frac{p}{n}}$
K_{NO}	0.020	0.0593	0.122	0.204
K_N	0	0	0	$2.21\times10^{-4}\sqrt{\frac{p}{n}}$
K_O	$6.64\times10^{-4}\sqrt{\frac{n}{p}}$	$0.0144\sqrt{\frac{n}{p}}$	$0.112\sqrt{\frac{n}{p}}$	$0.490\sqrt{\frac{n}{p}}$
K_{OH}	0.581	0.899	1.20	1.42
K_H	$1.62\times10^{-3}\sqrt{\frac{n}{p}}$	$0.0251\sqrt{\frac{n}{p}}$	$0.157\sqrt{\frac{n}{p}}$	$0.587\sqrt{\frac{n}{p}}$
n_{N_2}	1.879	1.875	1.860	1.840
n_H	0	0.011	0.129	0.639
n_{H_2}	0.009	0.066	0.214	0.319
n_O	0	0.003	0.049	0.274
n_{H_2O}	0.990	0.912	0.653	0.248
n_{OH}	0.003	0.033	0.136	0.233
n_{O_2}	0.003	0.020	0.060	0.084
n_{NO}	0.001	0.011	0.041	0.080
n_N	0	0	0	6.10^{-4}
n	2.866	2.931	3.142	3.717

TABLE 8
HEATS OF FORMATION

	Species	n_i	ΔH_f° kcal/mole	$n_i \Delta H_f^\circ$	$\Sigma n_i \Delta H_f^\circ$ kcal/mole
3600	H	0	--	0	
	O	0	--	0	
	H_2O	0.990	-60.15	-59.5	
	OH	0.003	8.8	0.03	
	NO	0.001	21.6	0.02	-59.5
4500	H	0.011	54.6	0.6	
	O	0.003	61.2	0.2	
	H_2O	0.912	-60.36	-55.0	
	OH	0.033	8.6	0.3	-53.7
	NO	0.011	21.6	0.2	
5400	H	0.129	54.9	7.08	
	O	0.049	61.4	3.01	
	H_2O	0.653	-60.53	-39.53	-27.4
	OH	0.136	8.4	1.14	
	NO	0.041	21.5	0.88	
6300	H	0.639	55.16	35.25	
	O	0.274	61.45	16.84	
	H_2O	0.248	-60.70	-15.05	
	OH	0.233	8.17	1.90	+40.6
	NO	0.080	21.33	1.71	

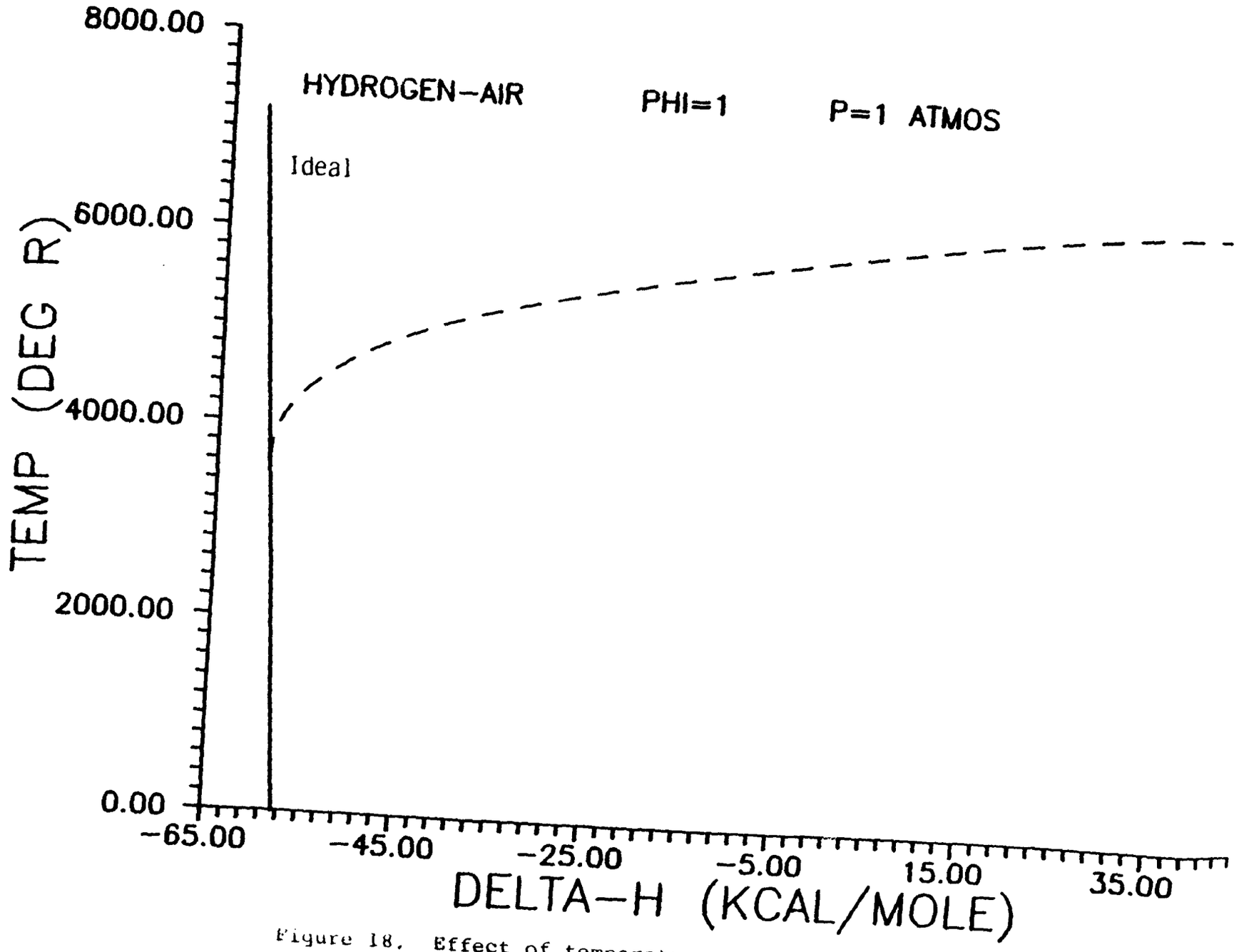

Figure 18. Effect of temperature on overall heat of combustion.

2.2.10.1 Non Reacting Flow Over Compression Ramp

Conditions for this test case were for two-dimensional laminar hypersonic flow over a 15.0 degree compression ramp (Figure 19). The present explicit computations were compared to the experimental results of Holden[16], the time-dependent computations of Hung and MacCormack[17], and the implicit MacCormack calculation of Lawrence, et al.[18] The conditions were:

$M_\infty = 14.1$	$Re = 1.04\times10^5$
$T_\infty = 72.2°K$	$T_w = 297.0°K$
$P_r = 0.72$	$L = 0.439$ m
$\sigma = 0.75$	$CDY = 0.025$

The computational grid consisted of 51 normal grid points geometrically spaced from 0.0 to 0.129L. As the computation was marched up the compression ramp, the grid was shifted by $\Delta\eta$ where

$$\Delta\eta = \Delta x \, \mathrm{Tan}(\theta_w)$$

The first point away from the body surface was located at a distance of $\Delta y_1/L=0.002$ and the marching step size ranged from one-quarter to three-quarters $\Delta y_1/L$. The SSCPNS code has proven to be extremely efficient in computing hypersonic flowfields. The above computation was performed in 2.2 seconds on a CRAY X-MP computer. This compares to a computation time of 1.72 seconds for the implicit calculation of Lawrence.

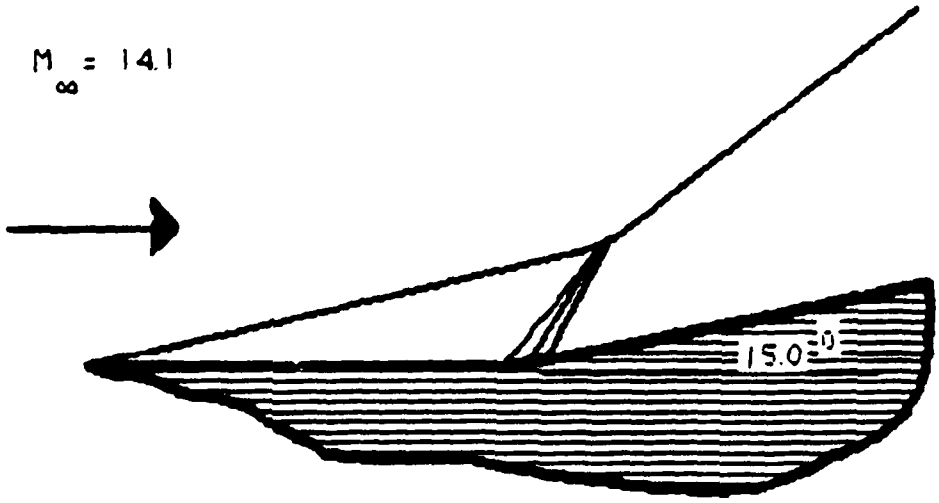

Figure 19. Ramp configuration for Holden's test cases.

For this test case, normal stress damping was introduced at solution initialization and then reduced by 0.5 percent per step. In addition, a small amount of second order smoothing was introduced to reduce oscillations. The following damping coefficients were used:

$$DNS1 = DNS2 = 0.25$$

Figure 20 depicts the surface pressure coefficient on the ramp surface, as a function of x, where C_p is defined as:

$$C_p = \frac{P}{\rho_\infty V_\infty^2}$$

Good agreement was obtained with Holden's experimental data and the FNS and PNS computations of Hung and MacCormack and Lawrence, et al., respectively. The Stanton number is plotted as a function of x in Figure 21; again note good agreement was obtained.

2.2.10.2 Experiment of Burrows and Kurkov

In the second test case the SSCPNS code was used to compute turbulent, two-dimensional, supersonic combustion flowfields. The test case conditions are those of the supersonic combustion investigation of Burrows and Kurkov.[19] A schematic of their experiment is shown in Figure 22. For their investigation, Mach 2.44 vitiated air is combusted with hydrogen. The hydrogen was injected with sonic speed through the small injection slot.

The computational grid used for this test case consisted of 81 points in the normal direction. The grid spacing in the normal direction was exponentially stretched to insure adequate resolution of the shear layer. A simple algebraic turbulence model (Baldwin-Lomax[20]) was incorporated to model the turbulent mixing.

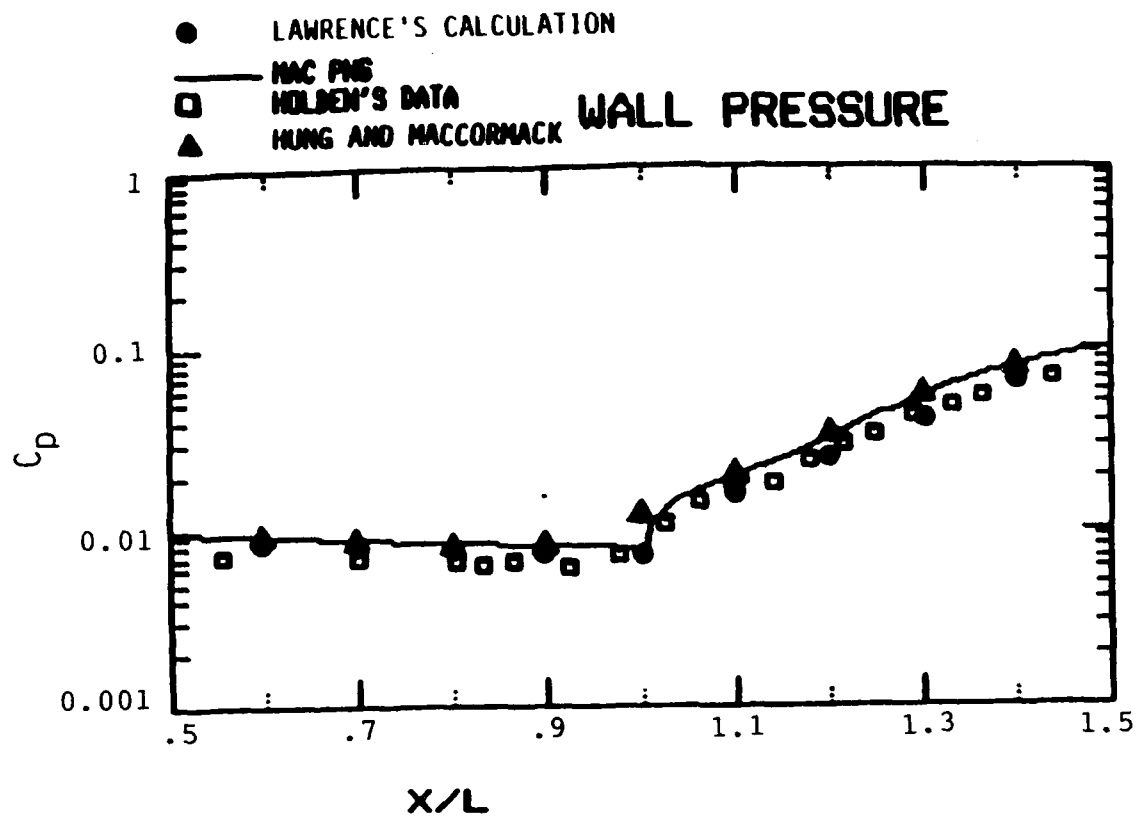

Figure 20. Wall C_p as a function of X. Holden's test conditions.

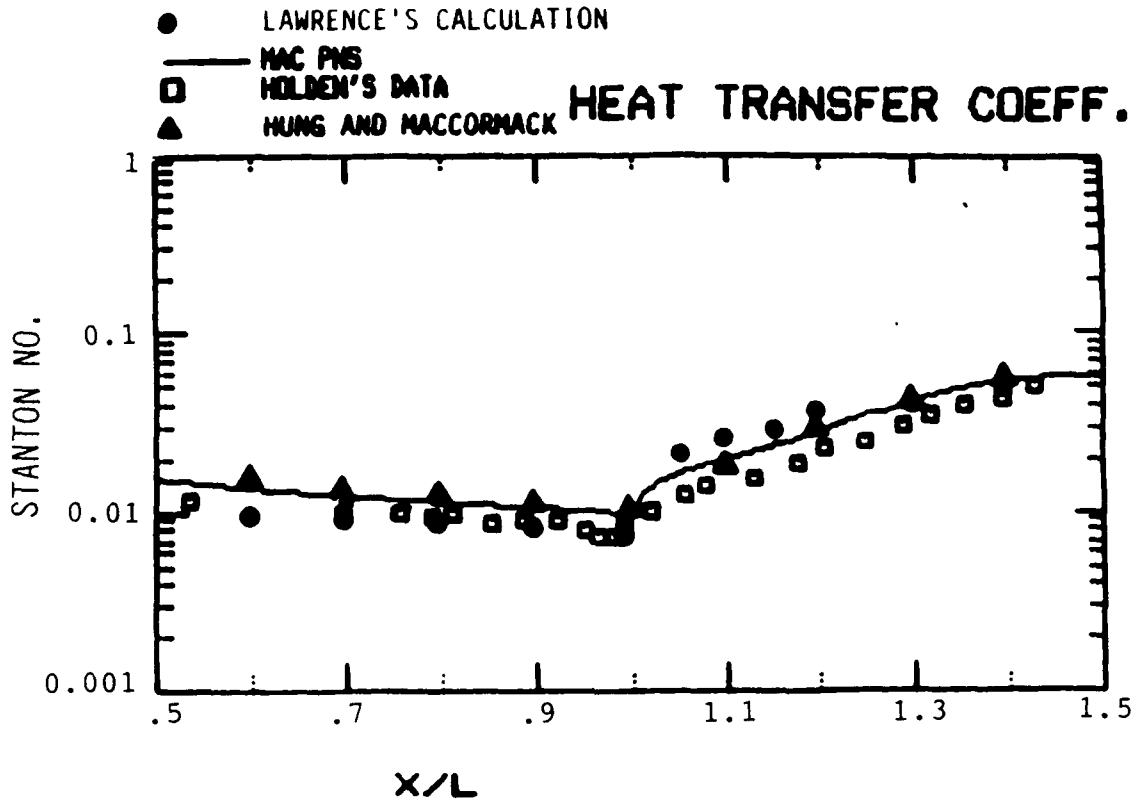

Figure 21. Comparison of heat transfer coefficients for Holden's test case.

TWO-DIMENSIONAL PNS WITH FINITE RATE AND EQUILIBRIUM REACTION RATE CHEMISTRY (BURROWS-KURKOV).

TURBULENT FLOW REGIME.

DIFFUSION CONTROLLED COMBUSTION.

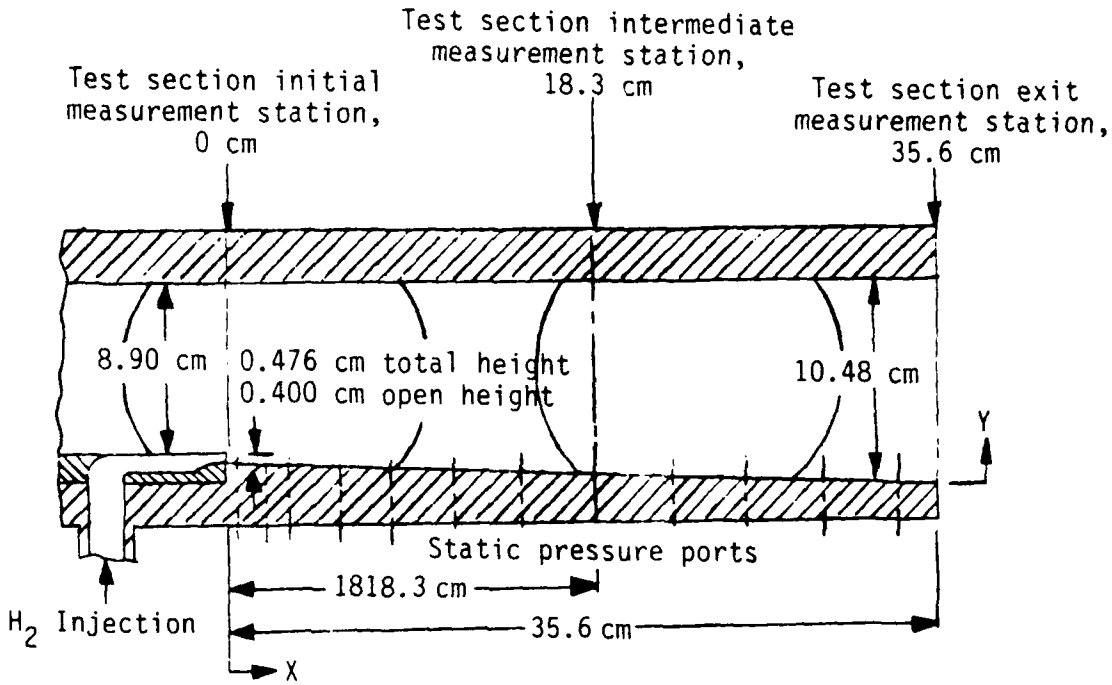

Test section showing hydrogen injection step, location of static pressure ports, and measurement stations.

Figure 22. Schematic of the Burrows-Kurkov Experimental Apparatus.

In this study, finite rate and equilibrium reaction rate models were employed when computing the Burrows-Kurkov test case. Figures 23 and 24 depict computed pressure contours (note the contour units are PSF) from the finite rate chemistry code (SSCPNS) and the equilibrium chemistry code (SSCPNSEQ). From the contour plots it is apparent that the results are quite similar except that the pressure rise associated with the combustion process is slightly lower in the SSCPNSEQ solution. This is attributed to the fact that for this particular test case the degree of reaction in the flame region was approximately 95 percent, thus accounting for the slightly lower pressure. The oscillations in the pressure contours near the upper wall were attributed to poor grid resolution in this region.

The computed static temperature contours from the SSCPNS and SSCPNSEQ codes are shown in Figures 25 and 26 respectively. As in the case of the static pressure contours, the computed temperature contours are quite similar except that the SSCPNSEQ solution predicts a slightly lower peak static temperature. This is to be expected since the SSCPNSEQ code allows for the backward chemical reactions. However, the maximum discrepancy between the two solutions was less than eight percent.

The computed mole fraction profiles from the SSCPNS and SSCPNSEQ codes are compared with the experimental data of Burrows and Kurkov, with good agreement, in Figures 27 and 28 respectively. The computed total temperature profile is shown in Figure 29. Again good agreement was obtained with experiment.

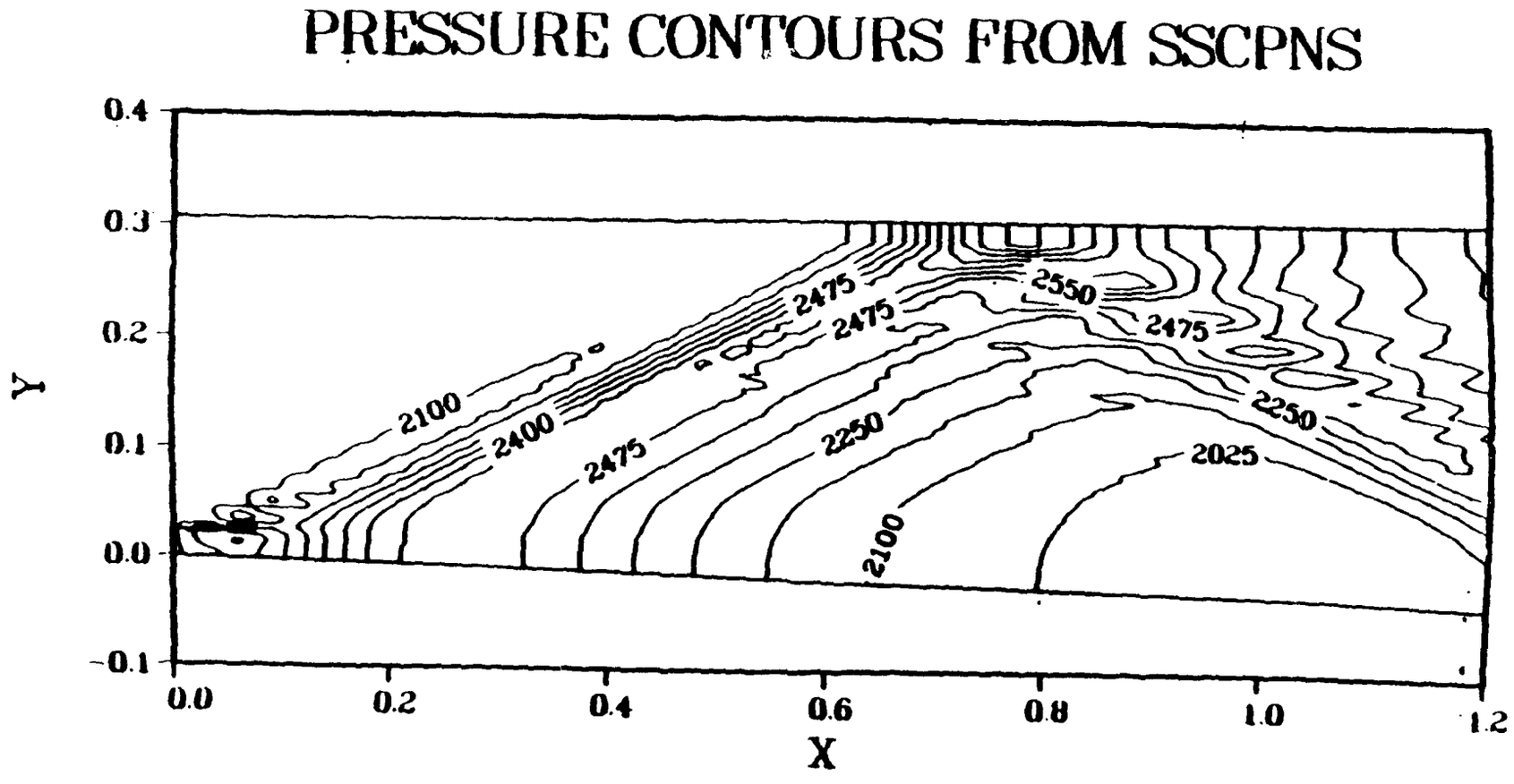

Figure 23. Computed pressure contours from the SSCPNS computer code (finite rate chemistry).

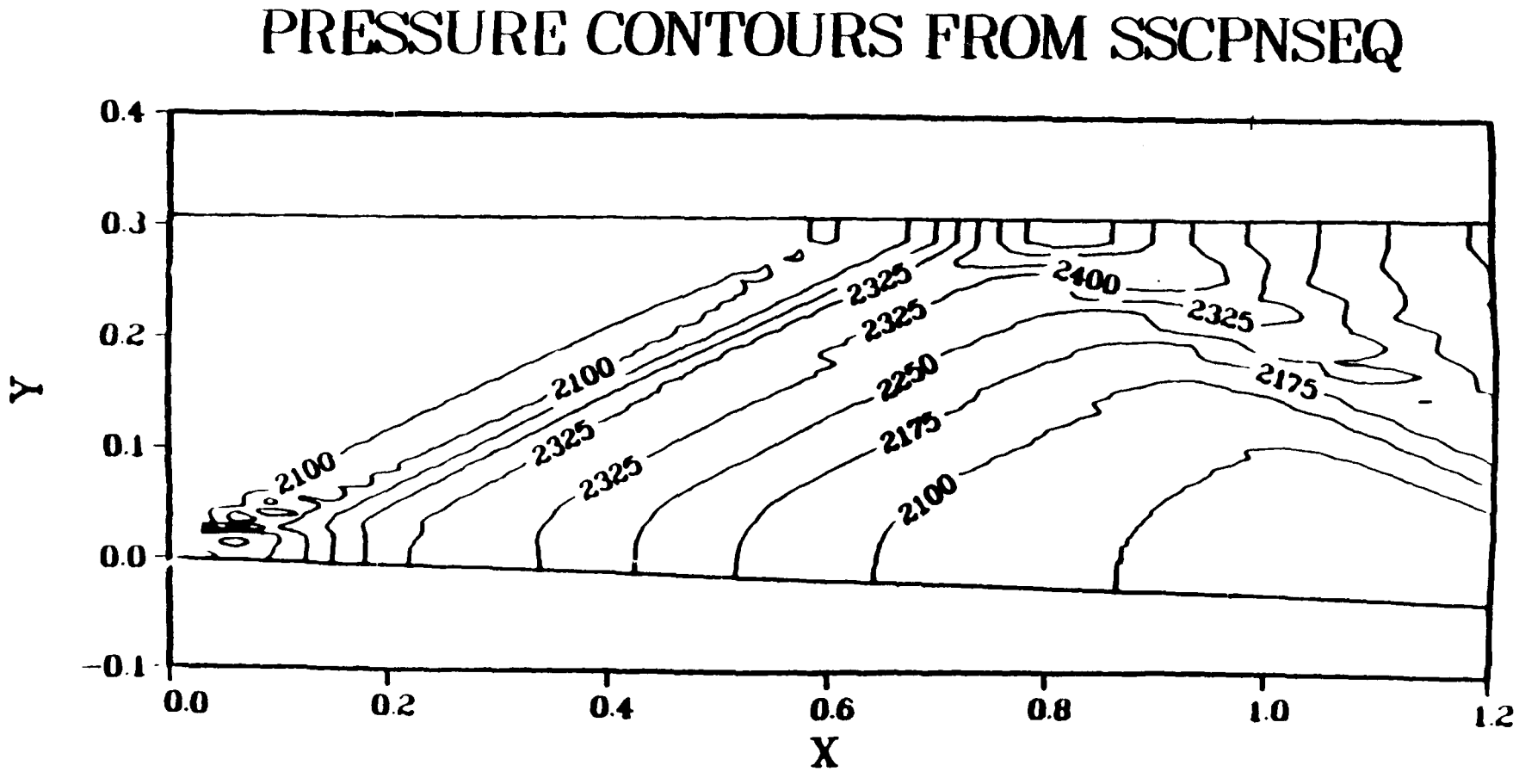

Figure 24. Computed pressure contours from the SSCPNSEQ computer code (equilibrium reaction rate model).

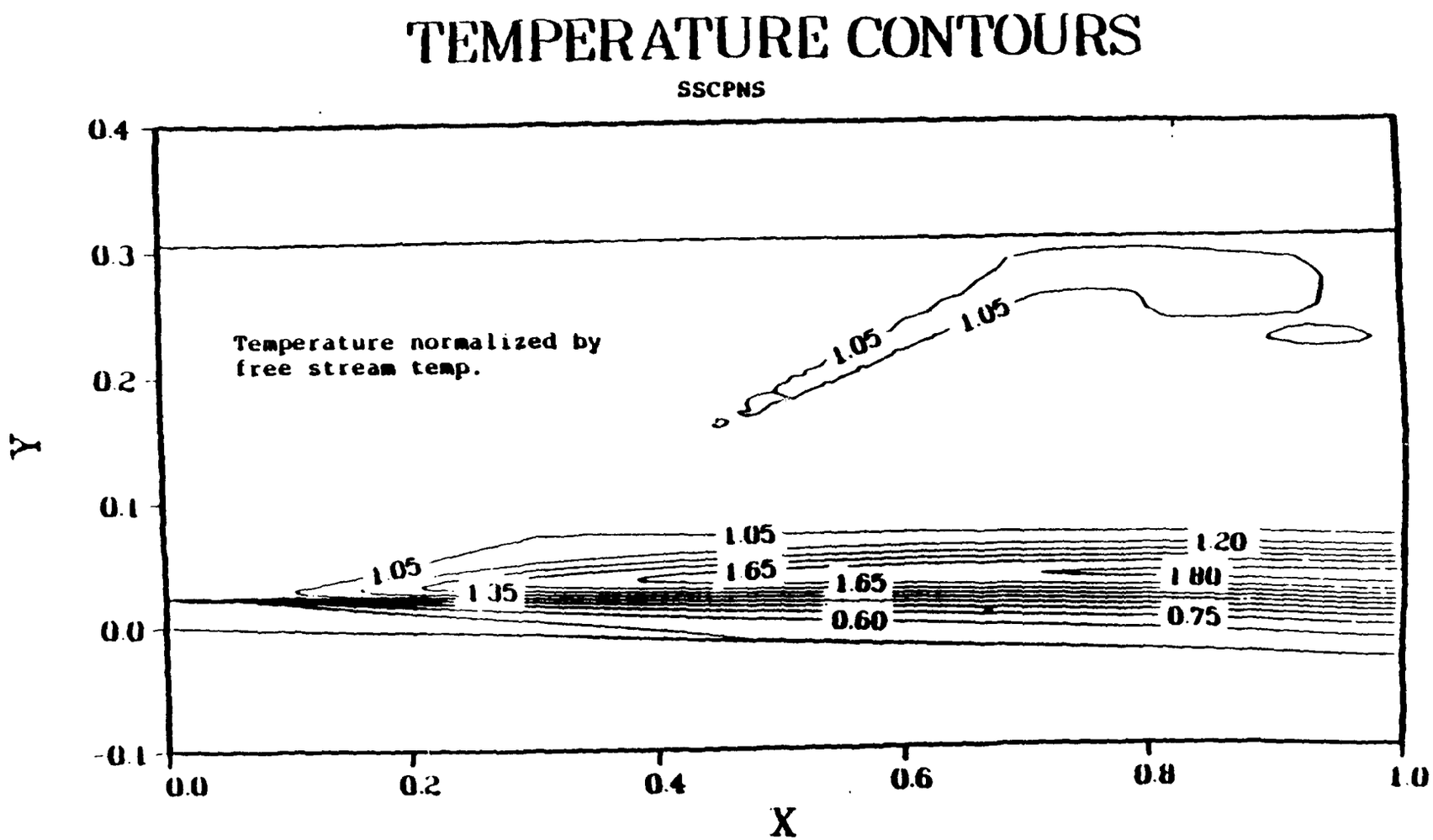

Figure 25. Computed temperature contours from SSCPNS.

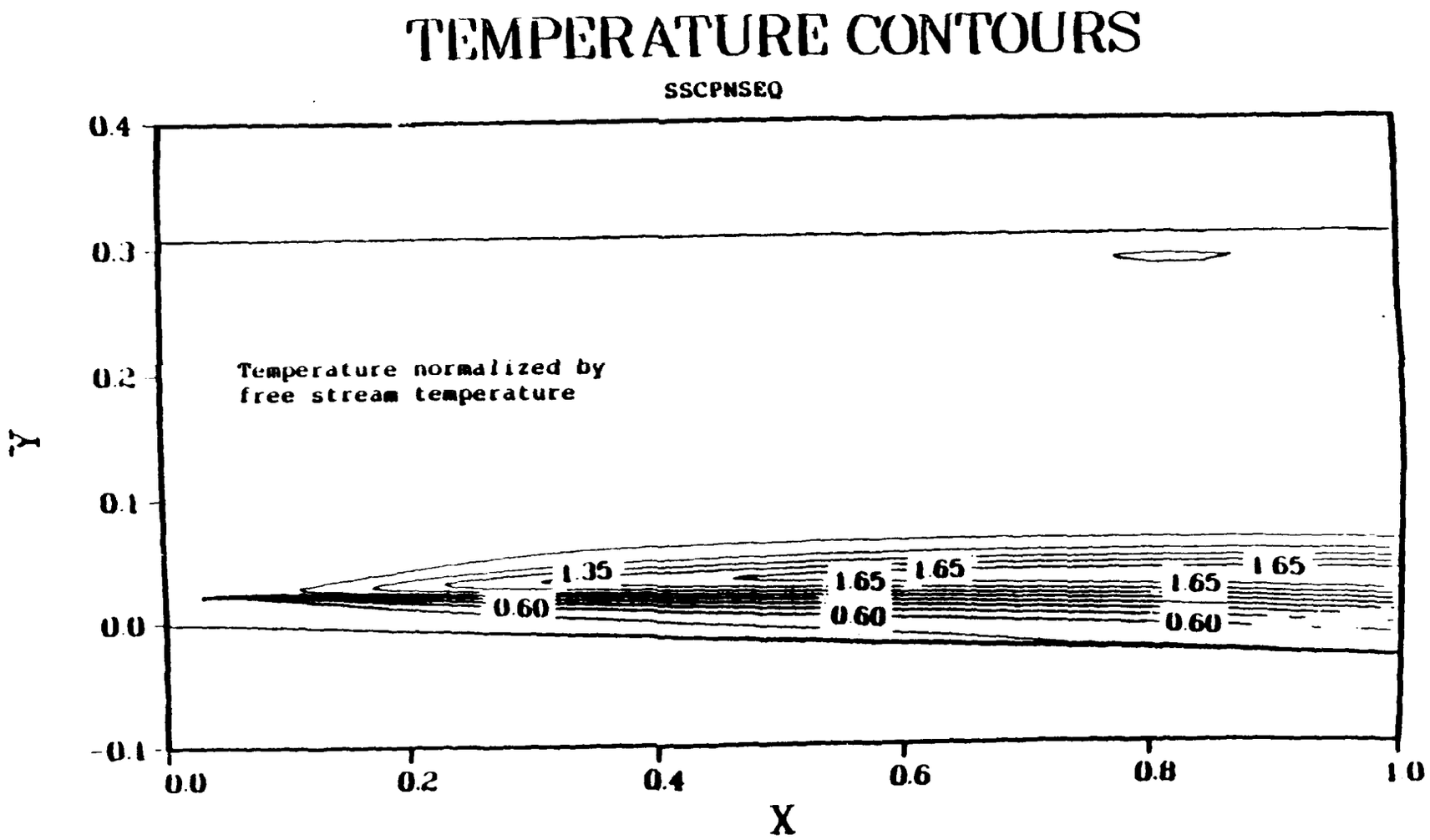

Figure 26. Computed temperature contours from SSCPNSEQ.

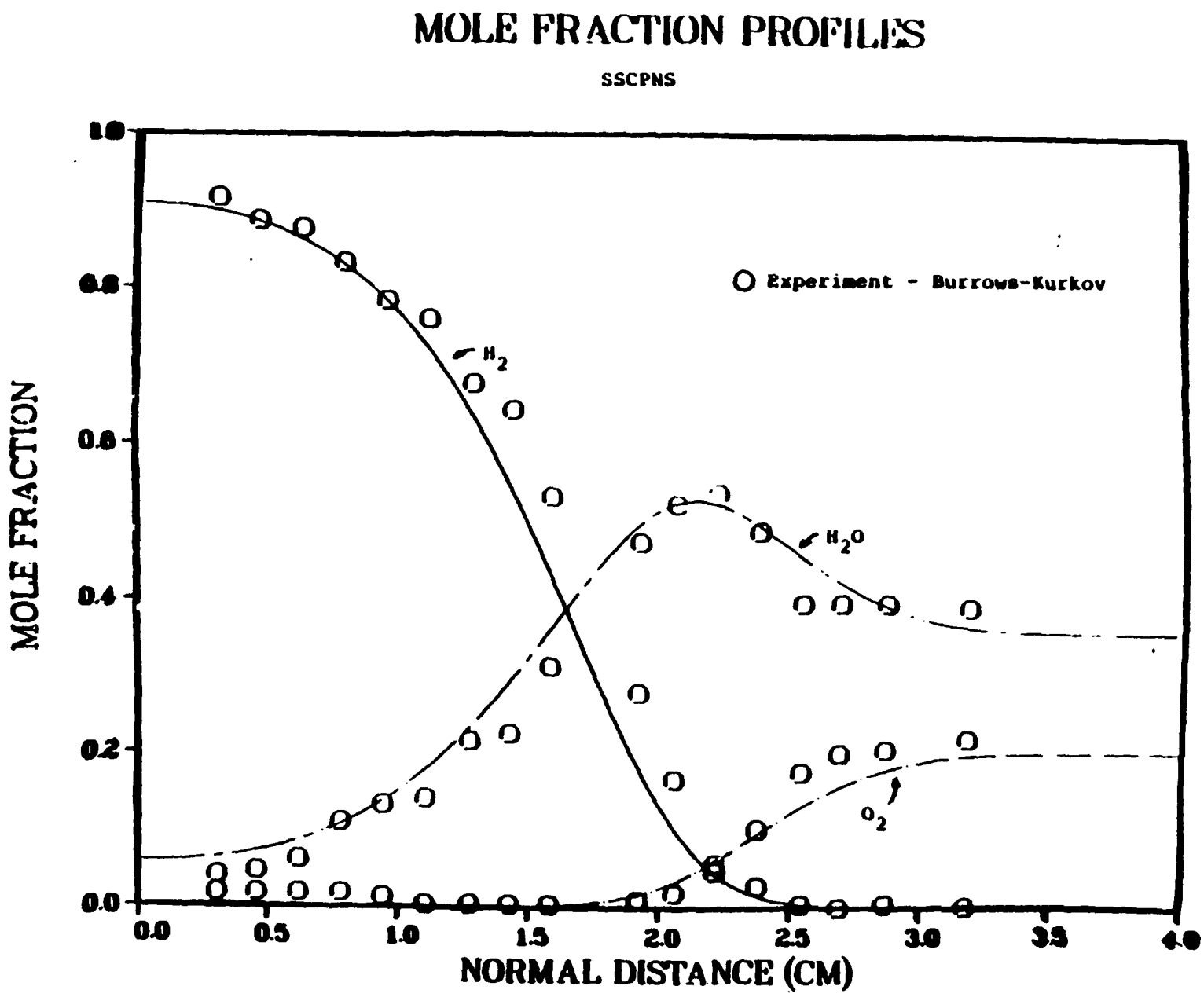

Figure 27. Comparison of computed and experimentally measured species mole fractions.

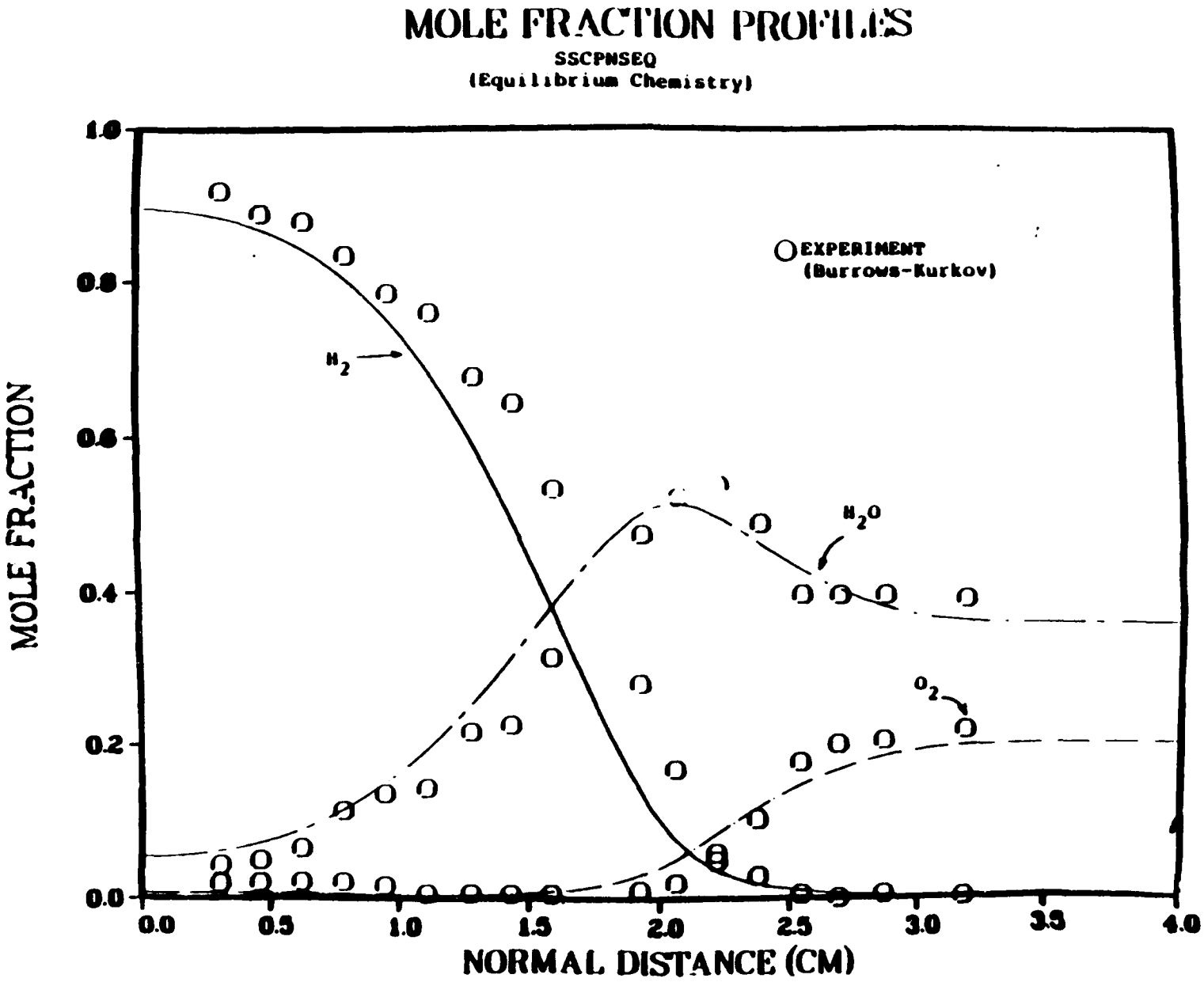

Figure 28. Comparison of computed and experimentally measured species mole fractions.

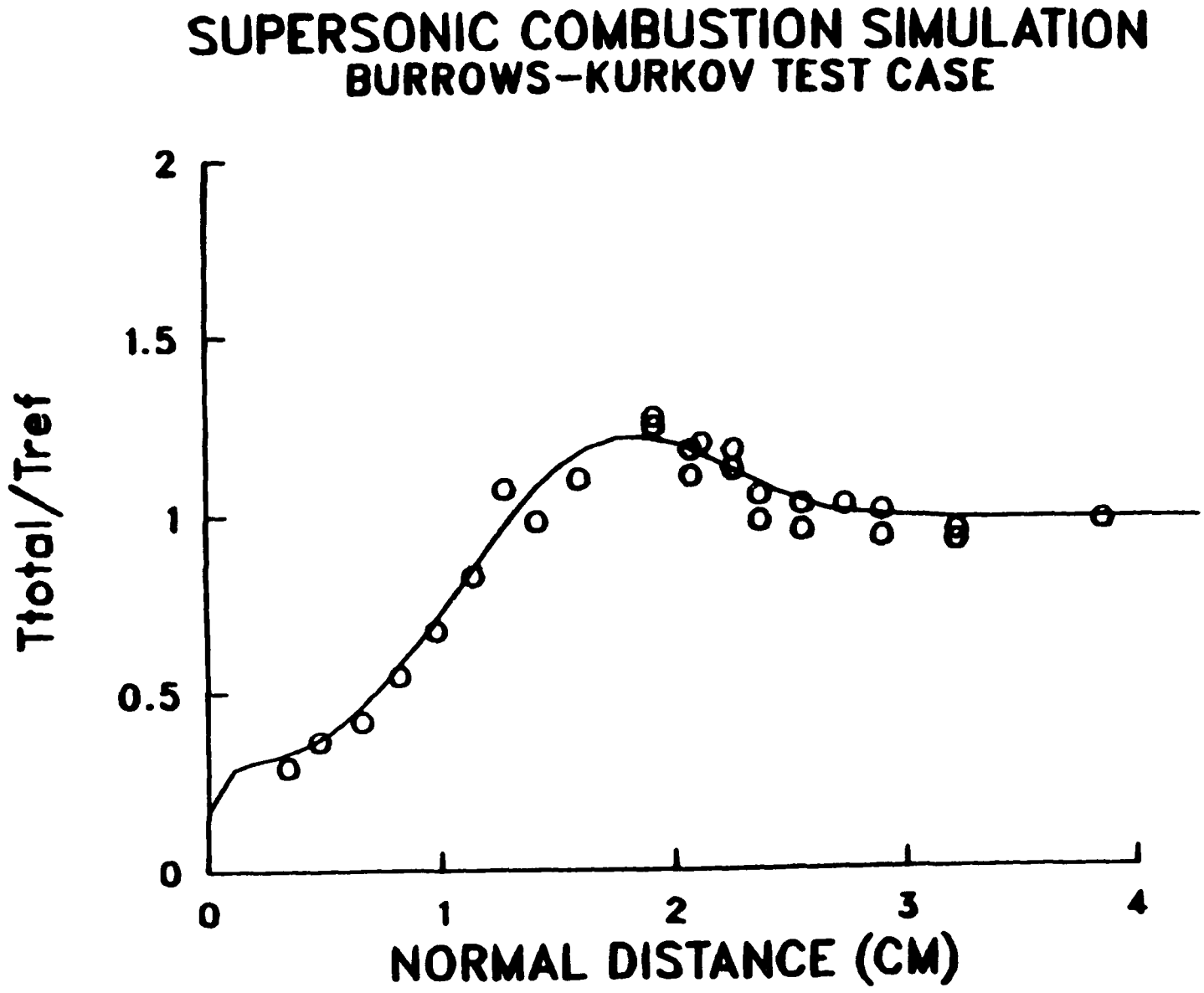

Figure 29. Comparison of computed and measured total temperature profiles. Varma's reaction rate model.

The SSCPNS and SSCPNSEQ computed solutions achieved good agreement with the data of Burrows and Kurkov. The primary difference between the SSCPNS and SSCPNSEQ computer codes is computational efficiency. The SSCPNS computer code performed the above computation in approximately 5 seconds on a CRAY X-MP computer while the SSCPNSEQ code required approximately 35 seconds to compute the calculation. The SSCPNSEQ reaction rate model is non-vectorizable and performs numerous table look-up operations when computing the degree of reaction. The SSCPNSEQ code should be used only when the peak temperatures predicted by the SSCPNS code are sufficiently high to cause shifts in chemical equilibrium.

The SSCPNS computer code has demonstrated capability to compute hypersonic, chemically reacting flowfields. The SSCPNS computer code has demonstrated good agreement with experimental data and the computations of others operating at flight conditions.

The SSCPNS formulations allow the above computations to be performed with little or no added dissipation. The SSCPNS code is ideally suited for vector processing, and has the potential for optimal parallel processing acceleration. The SSCPNS code performed the above computations accurately and economically, therefore, the SSCPNS code must be considered as a viable approach to computing hypersonic, chemically reacting flowfields.

This effort represents a preliminary study of the supersonic/hypersonic combustion phenomena in scramjet engines.

3. SUMMARY

This document reports on the computation of Ramjet Internal Flowfields. It is divided into two sections, i.e. subsonic and supersonic combustion. To numerically simulate subsonic combustion the time-dependent Navier-Stokes equations are used with additional species equations incorporated to model

hydrocarbon-air combustion. To compute supersonic combustion the parabolized Navier-Stokes equations (PNS) are utilized with species equations to simulate hydrogen-air combustion. Model cases are computed and compared with limited experimental data.

REFERENCES

1. Wilke, C. R., Journal of Chemical Physics, Vol. 18, pp. 517-519, 1950.

2. Kanury, A. M., Introduction to Combustion Phenomena, Gordon and Breach Science Publishers, New York, 1982.

3. JANNAF Thermochemical Tables: Dow Chemical Company, Midland, Michigan.

4. Shang, J. S., "Flow Oscillations of Spike-Tipped Bodies," AIAA Paper 80-0062, January 1980.

5. Coffee, T. T., Kotlar, A. J., and Miller, M.S., "The Overall Reaction Concept in Premixed, Laminar Steady State Flames. I. Stoichiometrics," Combustion and Flame, Vol. 54, pp. 155-169, 1983.

6. McRae, D. S.,"A Numerical Study of Supersonic Cone Flow at High Angle of Attack," AIAA Paper 76-97, 1976.

7. Eklund, D. R., Hassan, H. A., and Drummond, J. P., "The Efficient Calculation of Chemically Reacting Flow," AIAA Paper 86-0563, AIAA 24th Aerospace Sciences Meeting, Reno, Nevada, January 1986.

8. Vigneron, Y. C., Rakich, J. V., and Tannehill, J. C., "Calculation of Supersonic Viscous Flows Over Delta Wings With Sharp Subsonic Leading Edges," AIAA Paper 78-1137, 1978.

9. Thomas, P. D. and Lombard, C. K., "The Geometric Conservation Law-Link Between Finite Difference and Finite-Volume Methods of Flow Computations on Moving Grids," AIAA Paper 78-1208.

10. Gielda, T. P. and McRae, D. S., "An Accurate, Stable, Explicit Parabolized Navier-Stokes Solver for High Speed Flows," AIAA Paper 86-1116, 1986.

11. Gielda, T. P. and McRae, D. S., "Explicit Parabolized Navier-Stokes Solutions for Secant-Ogive-Cylinder-Boat-Tail and Finned Projectiles," AIAA Paper 87-2292, 1987.

12. MacCormack, R. W., "The Effect of Viscosity in Hypervelocity Impact Catering," AIAA Paper 69-354, 1969.

13. MacCormack, R. W. and Baldwin, B. S., "A Numerical Method for Solving the Navier-Stokes Equations With Application to Shock-Boundary Layer Interaction," AIAA Paper 75-1, 1975.

14. Stowers, S., "Species and Reactions Table," Personal communication from Steve Stowers, Pratt and Whitney, West Palm Beach, Florida.

15. Varma, A. K., Chatwani, A. J., and Bracco, F. V.,"The Overall Reaction Concept in Premixed Laminar Steady State Flames," Combustion and Flame, Vol. 64, pp. 223-226, 1986.

16. Holden, M. S. and Moselle, J. R., "Theoretical and Experimental Studies of the Shock Wave-Boundary Layer Interaction on Compression Surfaces in Hypersonic Flow," CALSPAN, Buffalo, New York, Report AF-2410-A-1., 1969.

17. Hung, C. M. and MacCormack, R. W., "Numerical Solution of Supersonic and Hypersonic Laminar Compression Corner Flows," AIAA Journal, Vol. 14, pp. 475-481, 1976.

18. Lawrence, S. L., Tannenhill, J. C. and Chaussee, D. S., "Application of the Implicit MacCormack Scheme to the Parabolized Navier-Stokes Equations," AIAA Paper 83-1956.

19. Burrows, M. C. and Kurkov, A. P., "Analytical and Experimental Study of Supersonic Combustion of Hydrogen in a Vitiated Airstream," NASA-TM-X-2828, 1978.

20. Baldwin, B. S. and Lomax, H., "Thin Layer Approximation and Algebraic Model for Separated Turbulent Flows," AIAA Paper 78-257, Huntsville, Alabama, 1978.

APPENDIX

EQUILIBRIUM COMPUTATIONAL PROCEDURES

In the aerospace application of combustion in advanced propulsion devices, a gaseous fuel jet is burned as it issues into air through a narrow injection nozzle at high velocity. Combustion of a fuel jet is known to be a diffusion limited process. The fuel in the jet and the inlet air are transported toward one another by convective diffusion. At all locations where the fuel and oxygen are in stoichiometric proportions, combustion takes place rapidly. In an ideal diffusion flame, the reaction zone is so thin that it could be considered as a surface of zero thickness impermeable to oxygen as well as fuel. In a hydrocarbon fuel flame the reaction zone is visibly blue (flame temperature about 2,000°K). As the carbon formed in the combustion process flows out of the reaction zone, it is usually incandescent (yellow). Far out of the flame, the soot cools down to lose incandescence. This feature is borne out in the movies taken of the Aero Propulsion Laboratory experimental test results of the dump combustor.

To mathematically model the combustion process of a diffusion flame, a chemically reacting mixture of gases must be addressed. When a mixture of reactants is placed in an enclosure and allowed to react, surprisingly not all reactants get consumed to yield products. This state in which reactions refrain from proceeding further is called chemical equilibrium. The composition depends upon temperature and pressure. The chemical equilibrium state is dynamic in nature rather than static, i.e., the reactions never cease to occur even at equilibrium. At equilibrium the rates of the forward and backward reactions are equal.

The computation of the equilibrium state involves a series of algebraic equations representing the conservation of elements and relationships for the equilibrium constants. An iteration scheme is used to solve for the single positive real root

produced by these algebraic relationships. Such a procedure would be impractical for time dependent calculations on an unsteady combustion simulation. Therefore, an alternate method is required, convenient for approximate simple reactions. The method adopted here is called the "extent of reaction" method. It is described herein for hydrogen/air combustion.

Extent of Reaction Method

Consider stoichiometric hydrogen-air reaction at any intermediate stage of completion, expressed by the fraction λ.

$$[H_2] + \frac{1}{2}[O_2+3.76N_2] \rightarrow (1-\lambda)\ [H_2+\frac{1}{2}O_2] + \lambda[H_2O] + \frac{1}{2}[3.76N_2]$$

This equation implicitly satisfies mass conservation. The information for this reaction is tabulated in the following table:

i	n_i	X_i	Y_i
H_2	$1-\lambda$	$\frac{2(1-\lambda)}{6.76-\lambda}$	$.028(1-\lambda)$
O_2	$.5(1-\lambda)$	$\frac{(1-\lambda)}{6.76-\lambda}$	$.226(1-\lambda)$
H_2O	λ	$\frac{2\lambda}{6.76-\lambda}$	$.255\lambda$
N_2	1.88	$\frac{3.76}{6.76-\lambda}$	.745

The single parameter λ may be determined from one equilibrium constant K_{H_2O} which is a strong function of temperature and weakly dependent upon pressure.

$$\sqrt{p}\ K_{H_2O}(T) = \frac{n_{H_2O}\ \sqrt{n}}{n_{H_2}\ \sqrt{n_{O_2}}} = \frac{\lambda\ \sqrt{6.760-\lambda}}{(1-\lambda)^{1.5}}$$

Hence, λ may be determined directly from the thermodynamic state variables of pressure and temperature.

The following table displays the mass fraction equilibrium values for the complete reaction of hydrogen-air versus the single equation model (extent of reaction method) for various temperatures at a pressure of one atmosphere.

TABLE OF MASS FRACTIONS

	Y_1				
i \ T	2000°K	2500°K	3000°K	3500°K	p=1 atoms
H_2	0	0.002	0.006	0.009	Complete Reaction Model
O_2	0.001	0.009	0.027	0.038	
H_2O	0.252	0.232	0.167	0.063	
H	0	0	0.002	0.009	
O	0	0	0.011	0.062	
OH	0	0.008	0.033	0.056	
N_2	0.745	0.743	0.737	0.729	
NO	0	0.005	0.017	0.034	
λ	0.9922	0.9431	0.8010	0.5747	Single Equation Model
H_2	0	0.002	0.006	0.012	
O_2	0.002	0.013	0.045	0.096	
H_2O	0.253	0.240	0.204	0.147	
H	0	0	0	0	
O	0	0	0	0	
OH	0	0	0	0	
N_2	0 /45	0.745	0.745	0.745	
NO	0	0	0	0	
λ_1	0.992	0.955	0.861	0.752	Two Equation Model
λ_2	0	0.0354	0.170	0.440	
H_2	0	0.002	0.006	0.012	
O_2	0.002	0.010	0.031	0.056	
H_2O	0.253	0.235	0.182	0.107	
H	0	0	0	0	
O	0	0	0	0	
OH	0	0.008	0.035	0.080	
N_2	0.745	0.745	0.745	0.745	
NO	0	0	0	0	

From the Table of Mass Fractions, fair agreement is observed ($\pm 4\%$) up to about 3000°K. Improvement in the model may be achieved by including additional species. However, each species requires one additional parameter, λ_i. It may be observed from the Table of Mass Fractions that the next species to include is OH. The following is the modification of the extent of reaction method for a two equation model.

To the original reaction an additional reaction equation is added.

<u>Reaction 1</u>

$$[H_2] + \frac{1}{2}[O_2+3.76N_2] \rightarrow (1-\lambda_1)\ [H_2+\frac{1}{2}O_2] + \lambda_1[H_2O] + \frac{1}{2}[3.76N_2]$$

<u>Reaction 2</u>

$$[H_2O] \rightarrow \lambda_2[\frac{1}{2}H_2+OH] + (1-\lambda_2)\ [H_2O]$$

Combining the two reactions produces the following equation:

$$[H_2] + \frac{1}{2}[O_2] \rightarrow (1-\lambda_1+\frac{1}{2}\lambda_1\lambda_2)[H_2] + \frac{1}{2}(1-\lambda_1)\ [O_2]$$

$$+ \lambda_1(1-\lambda_2)\ [H_2O] + \lambda_1\lambda_2[OH]$$

Two equilibrium constants are needed to evaluate λ_1 and λ_2:

$$\sqrt{p}\ K_{H_2O}(T) = \frac{n_{H_2O}\ \sqrt{n}}{n_{H_2}\ \sqrt{n_{O_2}}} = \frac{\lambda_1(1-\lambda_2)[6.76-\lambda_1(1-\lambda_2)]^{1/2}}{[1-\lambda_1+\frac{1}{2}\lambda_1\lambda_2]\ [1-\lambda_1]^{1/2}}$$

$$K_{OH}(T) = \frac{n_{OH}}{\sqrt{n_{H_2}}\ \sqrt{n_{O_2}}} = \frac{\sqrt{2}\ \lambda_1\lambda_2}{[1-\lambda_1+\frac{1}{2}\lambda_1\lambda_2]^{1/2}\ [1-\lambda_1]^{1/2}}$$

The information for this reaction is tabulated in the following table:

i	n_i	Y_i
H_2	$1-\lambda_1+\frac{1}{2}\lambda_1\lambda_2$	$0.0283\ (1-\lambda_1+\frac{1}{2}\lambda_1\lambda_2)$
O_2	$\frac{1}{2}\ (1-\lambda_1)$	$0.226\ (1-\lambda_1)$
H_2O	$\lambda_1\ (1-\lambda_2)$	$0.255\ \lambda_1(1-\lambda_2)$
N_2	1.88	0.745
OH	$\lambda_1\lambda_2$	$0.241\ (\lambda_1\lambda_2)$

A comparison of the two equation model with the one equation model and the complete reaction model is shown in the Table of Mass Fractions. The two equation model cuts the mass fraction error in half to about ±2% at 3000°K. Property errors of this magnitude are probably satisfactory for numerical simulation, however, a more serious difficulty exists. The mass fractions are used to establish the specific heats (to relate temperature and enthalpy) and to ascertain the total heat of formation for the reaction. A Table of Enthalpy permits comparison of the approximate models with the complete reaction.

The following is a summary of enthalpy errors.

ENTHALPY ERRORS

T(°K)	One Equation Model	Two Equation Model
2000	0.2%	0.2%
2500	0.3%	0.2%
3000	1.9%	0.9%
3500	6.5%	4.5%

TABLE OF ENTHALPY

P=1 atmos.	T(°K)			$Y_i h_i$
Molecule	2000	2500	3000	3500
H_2	0	30	130	230
O_2	10	170	630	1070
H_2O	4380	5490	5040	2330
H	0	0	30	140
O	0	0	150	990
OH	0	140	700	1450
N_2	10000	13200	16330	19400
NO	0	90	390	920
h(cal)	14390	19120	23400	26530
H_2	0	30	130	300
O_2	30	240	1060	2710
H_2O	4390	5680	6160	5430
H	0	0	0	0
O	0	0	0	0
OH	0	0	0	0
N_2	10000	13230	16500	19820
NO	0	0	0	0
h(cal)	14420	19180	23850	28260
H_2	0	30	130	300
O_2	30	190	730	1580
H_2O	4390	5560	5500	3950
H	0	0	0	0
O	0	0	0	0
OH	0	140	750	2070
N_2	10000	13230	16500	19820
NO	0	0	0	0
h(cal)	14420	19150	23600	27720

Again, it is apparent that the heat capacity of the mixture can be satisfactorily produced up to 3000°K with either model. This is not true for the heat of formation, however. A comparison with the Table of Heat of Formation shows the growth of large errors with both models as shown below:

HEAT OF FORMATION ERRORS

T(°K)	One Equation Model	Two Equation Model
2000	0.7%	0.7%
2500	6.0%	3.0%
3000	85%	60%
3500	204%	165%

Clearly, an improvement is required in order to obtain correct values for the heats of formation. Since the one equation model produces satisfactory mass fractions and specific heats, it is proposed that this one equation model be retained with modified heats of formation. The heat of formation for H_2O is -60.5 kcal/mole for the range of interest. The formation of trace species greatly reduces the heat of combustion and, in fact, produces positive values at 3500°K due to dissociation effects. The following is a table of the heats of combustion for stoichiometric hydrogen-air for the complete reaction model at three different pressures.

TABLE OF HEAT OF FORMATION

P=1 atmos.	T(°K)			$X_i h_i$	
Species	2000	2500	3000	3500	
H_2	0	0	0	0	Complete
O_2	0	0	0	0	Reaction
H_2O	-20630	-18770	-12590	- 4070	Model
H	0	+ 220	+ 2250	+ 9500	
O	0	+ 60	+ 980	+ 4500	
OH	+ 8	+ 90	+ 360	+ 500	
N_2	0	0	0	0	
NO	+ 11	+ 90	+ 280	+ 470	
Δh_f(cal)	-20610	-18300	- 8720	+10900	
H_2	0	0	0	0	Single
O_2	0	0	0	0	Equation
H_2O	-20750	-19400	-16160	-11350	Model
H	0	0	0	0	
O	0	0	0	0	
OH	0	0	0	0	
N_2	0	0	0	0	
NO	0	0	0	0	
Δh_f(cal)	-20750	-19400	-16160	-11350	
H_2	0	0	0	0	
O_2	0	0	0	0	
H_2O	-20750	-18950	-14280	- 7950	
H	0	0	0	0	
O	0	0	0	0	
OH	0	+ 100	+ 300	+ 850	
N_2	0	0	0	0	
NO	0	0	0	0	
Δh_f(cal)	-20750	-18850	-13980	- 7100	

HEATS OF COMBUSTION

P(atoms) \ T(°K)	2000	2500	3000	3500
	Δh_f kcal/mole of mixture			
0.5		-17.58	- 5.22	
1.0		-18.31	- 8.72	+10.9
2.0		-18.94	-11.50	+ 5.06
	X_{H_2O}			
0.5		0.302	0.178	
1.0	0.343	0.311	0.208	0.067
2.0		0.318	0.234	0.0995
	Δh_f kcal/mole H_2O			
0.5	-60.5	-58.21	-29.32	
1.0	-60.5	-58.87	-41.92	+163
2.0	-60.5	-59.56	-49.14	+ 50.8

By using a reduced value for the heat of formation as shown in the above table, all thermodynamics of the combustion flow may be simply modeled.

REFERENCES

Kanury, A. M., "Introduction to Combustion Phenomenon," Gordon & Breach, New York, 1982.

☆U.S.Government Printing Office: 1989 —648-056/04480